ORNL/TM-2023/3090

In Situ Monitoring Assisted Large-Scale Additive Manufacturing of Mild Steel and 316 Alloys for Nuclear Applications

Soumya Nag
Mithulan Paramanathan
Fred List
Thomas Feldhausen
Andrzej Nycz
Bill Carter
et al.

September 2023
M3CR-22OR0402031

OAK RIDGE National Laboratory

ORNL IS MANAGED BY UT-BATTELLE LLC FOR THE US DEPARTMENT OF ENERGY

ORNL/TM-2023/3090

Advanced Materials and Manufacturing Technologies Program

IN SITU MONITORING ASSISTED LARGE-SCALE ADDITIVE MANUFACTURING OF MILD STEEL AND 316L ALLOYS FOR NUCLEAR APPLICATIONS

Soumya Nag
Mithulan Paramanathan
Fred List
Thomas Feldhausen
Andrzej Nycz
Bill Carter
Dennis Brown
Lauren Heinrich
Kenton Blane Fillingim
Luke Meyer
Brian Jordan
Jason Mayeur
Peeyush Nandwana
Yousub Lee
James Haley
Vincent Paquit

September 2023
M3CR-22OR0402031

Prepared by
OAK RIDGE NATIONAL LABORATORY
Oak Ridge, TN 37831
managed by
UT-BATTELLE LLC
for the
US DEPARTMENT OF ENERGY
under contract DE-AC05-00OR22725

CONTENTS

LIST OF FIGURES

LIST OF TABLES

ABBREVIATIONS

AISI	American Iron and Steel Institute
AM	additive manufacturing
AMMT	Advanced Materials and Manufacturing Technologies
BD	build direction
BP-DED	blown powder directed energy deposition
DD	deposition direction
DED	directed energy deposition
EBSD	electron backscatter diffraction
FLIR	forward-looking infrared
GMAW	gas metal arc welding
HIP	hot isostatic press
ID	inner diameter
IR	infrared
LED	light-emitting diode
LTT	low–transformation temperature
LWAM	laser wire-feed additive manufacturing
NRC	US Nuclear Regulatory Commission
OD	outer diameter
RPV	reactor pressure vessel
SS	stainless steel
TCR	Transformational Challenge Reactor
TD	transverse direction
WAAM	wire arc additive manufacturing

ABSTRACT

The Advanced Materials and Manufacturing Technologies (AMMT) Program aims to develop cross-cutting technologies in support of a broad range of nuclear reactor parts and to maintain US leadership in materials and manufacturing technologies for nuclear energy applications. The overarching vision of the AMMT Program is to accelerate the development, qualification, demonstration, and deployment of advanced materials and manufacturing technologies to enable reliable and economical nuclear energy. One of its three goals is to target big challenges and game-changing technologies to realize the mission and vision of the AMMT Program.

Based on this context, this multiyear work scope focuses on understanding the current state of large-scale additive manufacturing (AM) technology for the deposition of 316L stainless steel materials for final components and mild steel for use in nuclear manufacturing processes. The targeted AM modality is directed energy deposition (DED), which is capable of fabricating components on the size scale of meters, including valves, pumps, and impellers that are challenging or difficult to source, especially when developing new systems or replacing obsolete components. Accordingly, the current report provides a baseline literature survey on structure–property relationships in mild steel and 316L alloys. Also, information on preliminary trials to date involving these two alloys show potential for printing parts with complex geometry and thin-walled structures, such as nuclear valve and the hot isostatic press (HIP) can, using wire-based (wire arc AM and hybrid AM), as well as blown powder, DED machines. This research is aimed toward (1) demonstrating the ability to fabricate large components for pressure boundary applications relevant to the nuclear community and nuclear manufacturing technology and (2) understanding the effect of different manufacturing technologies on AM can production and post-HIP material for nuclear applications.

Another target of this report is to compile various in situ monitoring tools that have been incorporated for different DED AM modalities to understand process variability during the entire fabrication process. This variability can be correlated with processing–structure–property response surfaces and would add confidence around process quality verification and, ultimately, component certification for nuclear applications.

1. INTRODUCTION

Nuclear power reactors in the United States are primarily light-water reactors, which include pressurized water reactors and boiling water reactors [1]. These nuclear reactors are constructed of pressure boundary components such as valves, piping, and pump casing, as well as the reactor pressure vessel (RPV). Typically, the RPV needs to withstand exposure to neutron radiation during the operation of a nuclear power plant. The service life of a nuclear power plant is dictated by the response of RPV steels (e.g., 300 grade stainless steel [SS], SA533 and SA508 low-alloy steels) to neutron radiation at operating temperatures and pressures [1]. Notably, forging is the current method of fabrication for these large pressure vessels. With next-generation nuclear reactors needing much larger units, one RPV can run into upper limits of the forging press capacity. One viable solution for these relatively large parts is to weld large forgings together to form a single pressure vessel.

Additive manufacturing (AM) is an alternate fabrication technique to build large-scale parts that demand much less production volume. Most conventional manufacturing techniques (e.g., drilling, milling, turning) are classified as subtractive because these techniques remove excess or unwanted material from a starting block of material. This process inherently creates waste and inefficiencies. In contrast, AM processes build up components layer by layer, which enables the possibility of designing and building incredibly complex parts. For example, tools and components can be customized and designed to be compatible with specific applications that require matching material signatures. As a result, AM deposits material only where it is needed, making very efficient use of time, energy, and raw materials [2].

The flexibility in 3D printing allows designers to place materials where needed or pursue systems outside traditional structures [3]. Indeed, with supply chain ailments with manufacturing large-scale parts in a conventional casting and forging route, AM provides a niche manufacturing opportunity. The scalability and individualization, coupled with part complexity and customization, of uniquely designed nuclear components make AM an economically viable solution. In fact, AM is the only manufacturing technique in which the process may be faster, cheaper, and more energy-efficient to produce a more complex part [2].

Another advantage of using this novel manufacturing technique is to evaluate, develop, and maybe deploy newer material solutions. Currently, nuclear energy continues to rely on materials developed nearly 50 years ago. With the integration of advanced manufacturing and computational sciences, researchers can expedite the analysis and confirmation of materials for nuclear environments [3]. The goal is to help democratize the technology, giving small, less resourced firms and entities the ability to produce goods at a faster pace and larger scale at a relatively affordable cost [4].

AM for nuclear applications increased significantly in the late 2010s because of rapid progress in technology, particularly with methods using metals and ceramics [5]. The US Department of Energy Office of Nuclear Energy Transformational Challenge Reactor (TCR) Program integrated many of the abovementioned attributes to accelerate the deployment of AM technologies to industry. Some of the past successes of AM in the TCR Program include (1) a double-walled 316L SS cladding structure that is additively manufactured using a laser powder bed fusion method and used for UO_2 fuel and (2) a binder jet–printed SiC fuel element with integrated cooling channels capable of accommodating uranium nitride tristructural-isotropic and SiC powder that then densifies using chemical vapor infiltration process [6].

As an example, AM can evidently be a disruptive technology and thus has been subjected to a very rigorous qualification and certification protocols by the Federal Aviation Administration [7,8]. Currently, the US Nuclear Regulatory Commission's (NRC's) interest is geared toward understanding the following aspects of AM [9]:

- Reliability of AM processing and quality of AM parts

- Properties of AM parts
- Structural performance of AM parts, including their inspectability
- Service performance and aging degradation of AM parts
- Comparison of performance of AM parts with conventional manufacturing process (benchmarking)

Notably, for large-scale manufacturing units such as RPVs, all parts in the United States must be designed and fabricated per the American Society of Mechanical Engineers *Boiler and Pressure Vessel Nuclear Code*, as well as any additional requirements imposed by NRC regulations [1].

Thus, understanding the now near- to long-term aspects of AM are critical toward its success (Figure 1.1) [10]. Qualification and regulatory acceptance will ultimately determine the breadth and scope of applications for these technologies. This determination would lead to code qualification and the standardization of the AM process, which is key toward its successful implementation in nuclear energy.

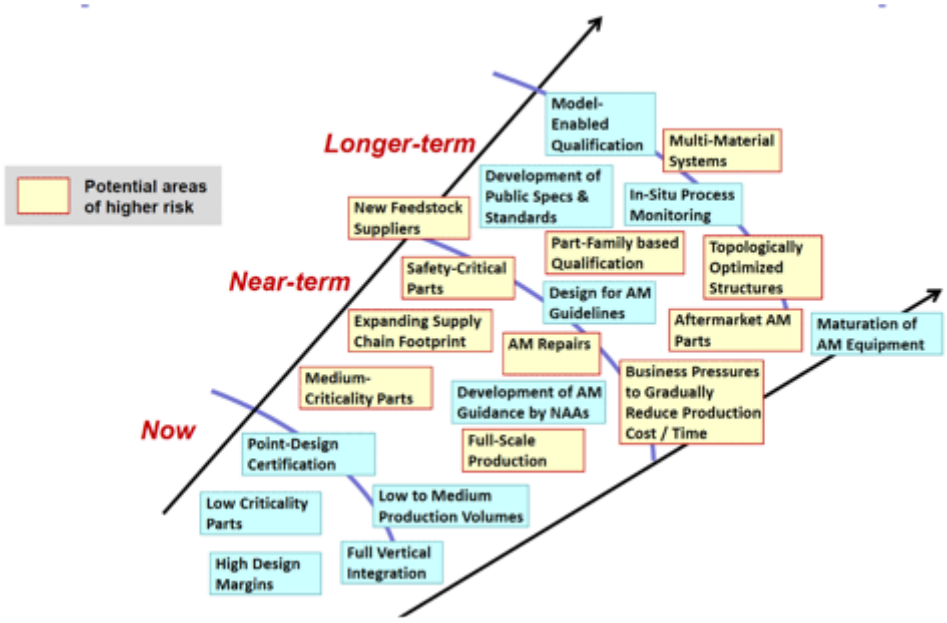

Figure 1.1. Expected evolution of AM landscape per "Regulatory Considerations for AM Qualification and Status of FAA AM Roadmap." [10]

Keeping these aspects in mind, this document provides a preliminary evaluation of additively manufactured pressure vessels using mild steel and 316L SS alloys. Section 2 is primarily a literature review of basic microstructural features, texture evolution, and defect variation, along with associated hardness and tensile property response in these two alloys. The modality of choice is directed energy deposition (DED) AM. Section 3 provides the gist of prominent large-scale AM modalities, with a focus on DED techniques. Three different manufacturing techniques were scoped out; wire arc AM (WAAM), hybrid AM, and blown powder DED (BP-DED) have been evaluated. In each case, challenges and opportunities to fabricate pressure vessel components (e.g. hot isostatic press [HIP] can) have been discussed. Section 4 discusses the state-of-the-art in situ monitoring setup and data collection options for each of the three DED modalities. All this information is extremely relevant toward the end goal of this work package: fabrication, inspection, testing, modeling, and, finally, certification of large-scale additively manufactured parts for nuclear applications.

2. STRUCTURE–PROPERTY RELATIONSHIPS OF LOW-CARBON STEELS FABRICATED BY DIRECTED ENERGY DEPOSITION TECHNIQUE: A LITERATURE REVIEW

2.1 CLASSIFICATION OF STRUCTURAL STEELS

In general, there are many ways of classifying steel in terms of structures, alloying elements, and carbon content. Based on the carbon content, structural steel can be categorized into four groups: (1) low- and mild-carbon steel, which has carbon content up to 0.25%; (2) medium-carbon steel with carbon content from 0.25% to 0.55%; (3) high-carbon steel with carbon content from 0.55% to 1.00%; and (3) ultrahigh-carbon steel with 1.0%–2.0% carbon content. Low-carbon steels possess moderate strength, high ductility, and lighter weight because of the low carbon content and addition of other alloys. These properties make low-carbon steel ideal for use in structural applications such as building construction, bridges, and transmission towers, where materials must be able to withstand high stress while also being easy to form into structural shapes.

2.2 CHARACTERISTICS OF MILD STEEL

Mild steel is an iron alloy with carbon as its main alloying element (usually between 0.16 and 0.25 wt %) [11]. It is one of the most widely used forms of steel and can be applied to a range of general-purpose applications. Mild steel owes its popularity to its adequate strength at low cost, in addition to its excellent machinability and weldability. Various grades of mild steel have differing amounts of carbon, with higher carbon contents wrestling in increased strength at the expense of ductility (Figure 2.1) [12]. In some cases, additional alloying elements such as manganese, phosphorus, and sulfur are added to improve properties such as weldability, tensile strength, corrosion resistance, and wear resistance.

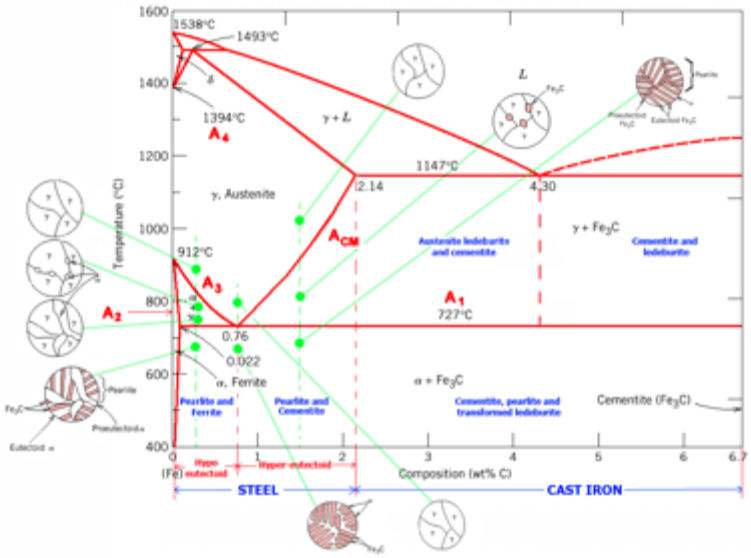

Figure 2.1. The iron–carbon phase diagram. [12]

The density of all grades of mild steel hovers near 7.8 g/cm^3. Alloys that fit under the mild steel umbrella that contain small amounts of alloying elements other than iron will have slightly different densities. The temperature at which mild steel becomes completely liquid varies between 1,450°C and 1,530°C, depending on the carbon and alloy content of the particular grade of steel.

2.2.1 Microstructure of Directed Energy Deposition Mild Steel

In WAAM of these geometries, the layer-by-layer buildup approach leads to repeated heating of already-deposited layers, which affects the mechanical properties of the parts to be manufactured [13–15]. Depending on the geometry or the surface-to-volume ratio of the part to be produced, different temperature profiles are formed. Steel transforms during cooling from high temperatures from face-centered cubic (FCC) γ austenite to body-centered cubic (BCC) ferrite at room temperature and carbides with different morphologies. In the case of fast cooling rates, this transformation results in the generation of martensite or lower bainite, but slower cooling rates promote the formation of upper bainite, pearlite, or ferrite [16]. Usually, the cooling rate and temperature range are of particular interest because the time for cooling from the austenite area is one of the main influencing factors regarding the microstructure and, thus, the mechanical properties. Further research by Colegrove et al. [17] demonstrated a microstructural change of WAAM mild steel via grain refinement and released residual stresses near the baseplate (which is a known challenge of the WAAM approach) using high-pressure rolling. Ding et al. [18], on the other hand, modeled the thermomechanical properties of mild steel WAAM structures to predict their residual stresses and associated distortion.

A microstructure delineation is visible at the weld line interface, as seen in Figure 2.2 [19]. Optical micrographs for a typical mild steel sample offer a representative microstructure seen throughout the build [19]. A typical ferrite microstructure is seen with small regions of pearlite at the grain boundaries. Grain coarsening is observed in some areas, but no clear delineations are observed at this scale between weld layers.

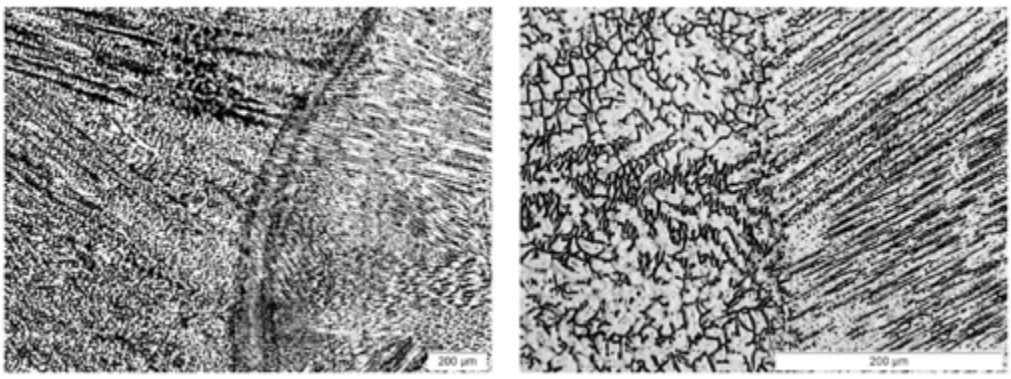

Figure 2.2. Optical micrographs of the interfacial layers between (left) weld lines and (right) repeating microstructural shifts observed near weld interfaces in AM SS 304 [17].

The typical electron backscatter diffraction (EBSD) and pole figures at the two end locations along the build height of a low–transformation temperature (LTT) steel (equivalent to low to medium carbon containing steels) is shown in Figure 2.3 [20]. BCC iron (martensite) was the majority phase observed in the specimen, with very small amounts of retained FCC iron (austenite). Overall, the microstructure across the high and low ends of the sample is similar, indicating a uniform microstructure that may be obtained via this fabrication method. The inverse pole figure maps along the height direction and the corresponding pole figures indicate a preferential texture along the height direction [20].

The large thermal gradients are the primary sources of residual stress formation in the additively manufactured parts, more so for parts built via the DED technique. Residual stresses exist within a body without any externally applied loads (i.e., the body is in equilibrium with its surroundings) [21, 22]. They are also referred to as *internal* or *locked-in* stresses, and they can either strengthen a material, such as toughened glass [23], or weaken a part. In AM, residual stress is often caused due to steep thermal gradients

within a part during its manufacturing process. According to Shorr [24], thermal stresses are generated when a nonuniform temperature field causes localized thermal expansion that is interfered with by nonexpanding (or less expanding) surrounding material, bodies, or parts. Residual stresses are classified based on the size of their effects: macro- vs. microstresses [22]; or *type I*, *type II*, and *type III* stresses [21, 25, 26]. Type I stresses, or macrostresses, act over large lengths with respect to the dimensions of the part. Type II stresses act over distances at the grain-size level and are often associated with phase transformations. Type III stresses are at the atomic scale (e.g., dislocation stress fields and crystal lattice defects) [26, 27]. Ding et al. [18] manufactured a thin wall of mild steel using the WAAM process with a modified gas metal arc welding (GMAW) heat source. Stresses in the sample were measured via neutron diffraction and the time-of-flight approach. An important finding was that the stresses in the longitudinal direction (parallel to the weld direction) were dominant over normal and transverse-directed stresses. It was also observed that distortions and stress redistribution occurred after the sample was unclamped from the baseplate [18]. The WAAM-processed mild streel samples were also investigated by Colegrove et al. [17], who also used neutron diffraction to characterize the residual stress. After adding each layer, rollers were applied to relieve residual stress and deformation; a profiled roller matched the surface shape of the deposited layer, and a slotted roller prevented lateral distortion. Results similar to Ding et al. [18] for the stress distribution were reported, reaching nearly 600 MPa [17] for the unrolled or as-built case, as shown in Figure 2.4.

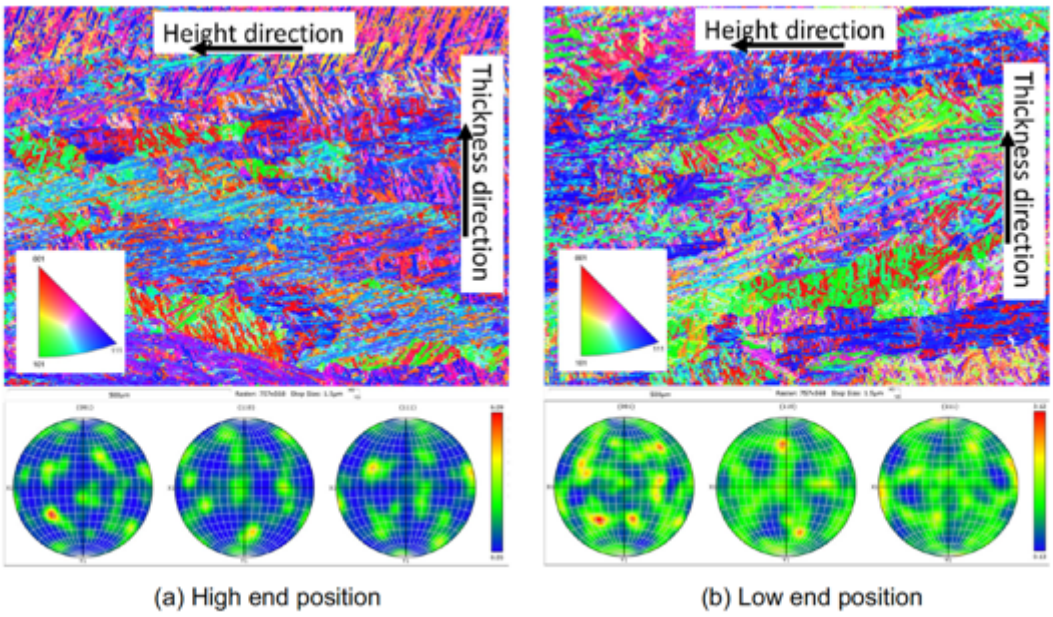

Figure 2.3. EBSD and pole figures at the high- and low-end positions of a WAAM-built LTT steel specimen [20].

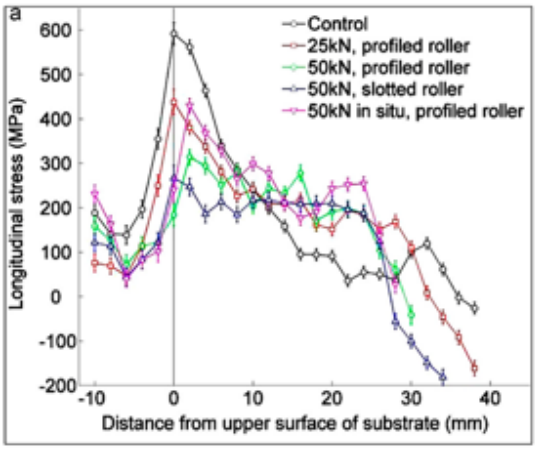

Figure 2.4. Longitudinal residual stress distribution through the depth of a specimen [17, 18].

2.2.2 Mechanical Properties of Directed Energy Deposition Mild Steel

Because the WAAM process is layer-based, the most critical area is the one located at the overlapping of the two layers or as close as possible to it. Brinell hardness of samples fabricated by a conventional metal inert gas process provided the biggest thermal input and minimum hardness variation, and the cold metal transfer process with the lowest thermal inputs provided an adequate dispersion among values, exhibited by their higher variation [27]. The average hardness values are presented in Figure 2.5, along with the average thermal input values. Usually, a homogenous hardness profile is desirable because it implies that the mechanical properties obtained by the WAAM process is uniform.

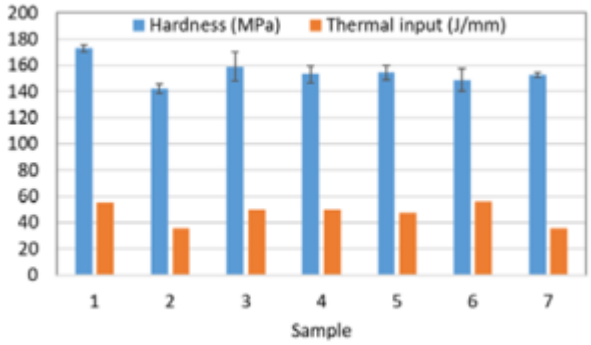

Figure 2.5. Mean Brinell hardness values and corresponding thermal inputs of large-scale AM mild steel specimens [27].

Similar to hardness, there is significant microstructural influence on tensile properties of large-scale additive builds (via WAAM or laser-based DED techniques). Thus, orientation-dependent phenomena are observable where tensile properties can vary depending on pull direction with respect to build direction.

Notably, because of differences in cooling rates and geometrical challenges, traditional comparisons with welding and standards may not yet apply to large-scale AM. Figure 2.6 shows the tensile stress–strain curves for three different orientations with reference to the build direction: perpendicular (90°), 45°, and parallel (0°) to the build direction [28]. The samples from the interface region of the build have the highest yield point (approximately 420 MPa, with red and orange curves). This region (bottom 50 mm) is generally

removed and discarded and is not typically associated with a structural component. The yield point drops to an average of 360 ± 7 MPa (black curves) in the remainder of the build for all orientations.

Tang et al. conducted a careful study of the temperature-dependent structure–property relationship in LTT steels (with low to medium carbon additions) that were fabricated by WAAM [20]. In their study, as shown in Figure 2.7, room-temperature results (24°C) are included in both figures, and dotted lines at 240°C and 640°C highlight the strength changes at the martensite start temperature (Ms) and austenite start temperature (As), respectively. The mechanical test results show a clear correlation with the hysteresis in the austenitic and martensitic phase transformations on heating and cooling, respectively. The elongation in both longitudinal and horizontal orientations show an overall increase with temperatures above 400°C but an obvious decrease in ductility at 350°C.

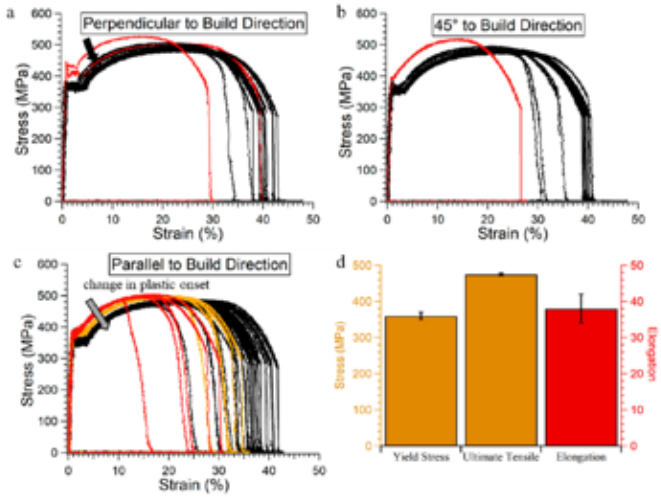

Figure 2.6. Stress–strain curves of specimens that are tested (a) perpendicular (90°), (b) 45°, and (c) parallel (0°) to the build direction. (d) Average yield strength, ultimate tensile strength, and elongation properties [28].

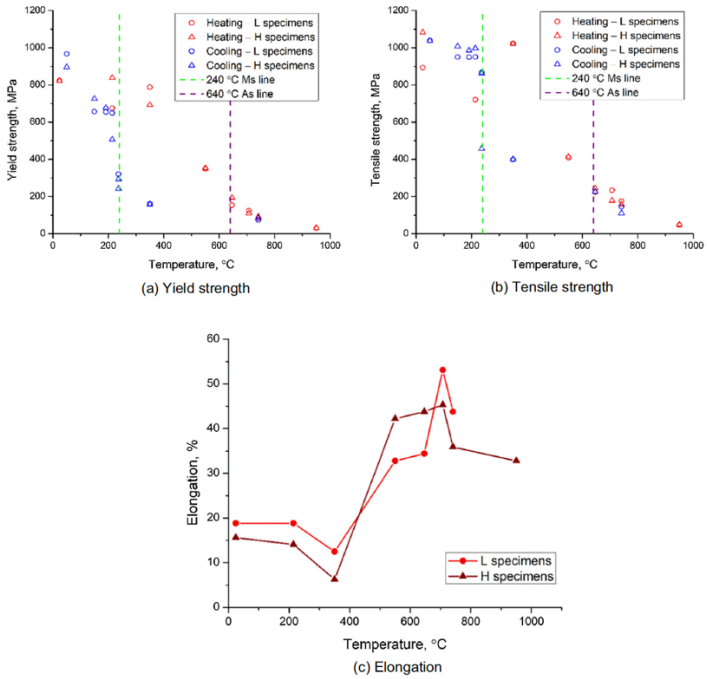

Figure 2.7. Tensile properties observed during the heating and cooling process of LTT steel specimen along (longitudinal) and perpendicular (horizontal) to the build direction (a) yield strength, (b) tensile strength, and (c) elongation [20].

2.3 CHARACTERISTICS OF 316L

Stainless Steel (SS) is a broad category of steel alloys that have some proportion of chromium that protects the metal from corrosion and related damage. The amount of chromium in the alloy—as well as the amounts of other metallic elements—differs depending on which variation of SS being worked with. 316 SS is a popular alloy that possesses molybdenum (Table 2.1).

Table 2.1. Composition ranges for 316L SS [12, 30].

Grade	Composition	C	Mn	Si	P	S	Cr	Mo	Ni	N
316L	Min.	—	—	—	—	—	16.0	2.00	10.0	—
	Max.	0.03	2.0	0.75	0.045	0.03	18.0	3.00	14.0	0.10

316 SS possesses enhanced resistance to corrosion from chloride and other acids [29]. This resistance makes it ideal for outdoor applications in marine environments or applications that risk potential exposure to chloride. One of the varieties of the 316 alloy class is 316L SS, which possesses less carbon and molybdenum than typical 316 steel. 316L is the superior choice for high-corrosion and high-temperature applications [30]. To qualify as 316L SS, the amount of carbon cannot exceed 0.03%. This amount decreases the risk of carbon precipitation, making it a better option for welding to ensure maximum corrosion resistance.

2.3.1 Microstructure of Directed Energy Deposition 316L

To date, several research studies have been carried out to determine the most effective type of heat transfer mechanism and, consequently, the cooling rate within the American Iron and Steel Institute (AISI) 316L components produced by DED [31,32]. As an example, Saboori et al. showed that in an AISI 316L sample, different heat transfer mechanisms dominate in different zones of a melt pool with the formation of various microstructural features [31]. Figure 2.8 reports the general microscopic images of the representative microstructures of as-built AISI 316L samples produced via DED [33]. The first visible feature is the curved border of melt pools, which is the typical AM microstructural characteristic as a consequence of the Gaussian distribution of laser energy (Figure 2.8a). The temperature gradients in the direction perpendicular to the curved melt pool borders are clearly intense and accordingly lead to the formation of a marked directional growth of the dendrites from the melt pool borders and converging toward the center of the melt pool (Figure 2.8b). On the contrary, at the central part of the melt pool, owing to the change of heat transfer mode, equiaxed dendrites are more likely to form. Regarding the whole section of the deposited component, because of the complex heat transfer during the DED process of this alloy, the columnar structure growing in the direction of the maximum thermal gradient is found to dominate in the middle height of the sample, whereas in the last deposited layers, an equiaxed cellular structure is present (Figure 2.8c–e) [31]. Additionally, during deposition, owing to the reheating of previously deposited layers, the middle area is also exposed to cyclic reheating that results in the formation of a heat-affected zone, which remains at higher temperatures for a longer time period. Thus, a finer microstructure and higher microhardness are expected for the bottom and top of the DED components, which undergo higher cooling rates with respect to other areas.

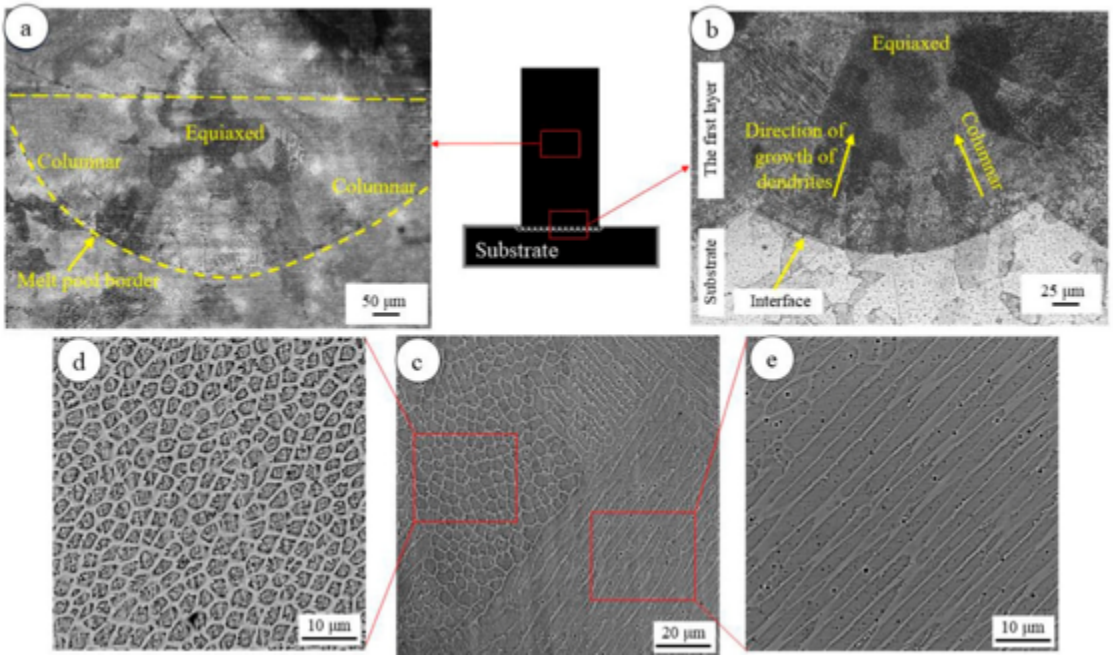

Figure 2.8. Light optical microscopy images of 316L steel samples produced by DED: (a) a representative melt pool at the middle height, (b) the microstructure of the first layer, (c) scanning electron microscopy images of columnar and equiaxed microstructures in the last deposition layer, and (d, e) higher magnifications images of the two regions [33].

The build orientation effect is distinctly observed in EBSD experiments, which are often used to characterize the grain morphology and crystal orientations. The results are visualized in Figure 2.9(a) and Figure 2.9(b) for the cross sections containing transverse direction (TD)–build direction (BD) and

deposition direction (DD)–BD, respectively [34, 35]. The approximate fusion zone interfaces are also indicated in the TD–BD cross section [Figure 2.9 (a)] by the dashed black lines. In both cross sections, large columnar grains (~50 to 100 µm in the shortest grain axis) are present. In the TD–BD cross section [Figure 2.9(a)], the columnar grain direction varies within a single fusion zone. Two characteristic regions can be identified: (1) the overlapping region between two neighboring fusion zones in a single layer and (2) the center of the fusion zone. These regions correspond to the left and right side of the image, respectively. In the overlapping region, the columnar grain direction is mostly aligned with the building direction, and the grains typically span multiple fusion zone interfaces, leading to large grains with large aspect ratios (i.e., the ratio between the major and minor axis lengths). In the fusion zone center, more variation exists in the columnar grain direction. Here, this direction is mainly aligned to the closest fusion zone interface normal, which varies significantly in this region. In the center of the fusion zone, the local temperature gradient (and, thus, the local grain growth direction) varies spatially; however, this correlation between grain morphology and grain orientation still holds. The aspect ratio of grains in this region is also smaller than for grains in the overlapping region. Both in the fusion zone center and in the overlapping region, the grain columnar direction is in accordance with the local temperature gradient during solidification [36], which promotes the columnar grain growth in these directions. Note that the EBSD data shown in Figure 2.9(b) are obtained for a DD–BD cross section in the overlapping region between two neighboring fusion zones, in which the grains are aligned with the building direction, as also observed in that region in Figure 2.9(a). Also, from Figure 2.9(b), it is evident that almost all grains in this cross section have one of their ⟨100⟩ easy-growth directions aligned with the building direction. As a consequence, a strong correlation exists between the columnar grain shape direction and the easy-growth ⟨100⟩ direction of the crystal.

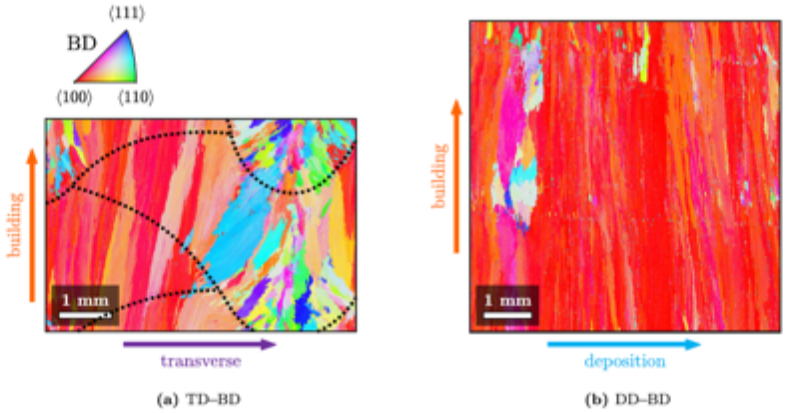

Figure 2.9. EBSD data of WAAM-produced 316L SS in two cross-sectional planes: (a) TD–BD and (b) DD–BD. In (a), the dashed lines indicate the approximate fusion zone interface. The EBSD data shown in (b) are obtained from a cross section in the overlapping region between two neighboring fusion zones [35].

In the 316L alloy, similar to mild steel, the dynamic nature of thermal phenomena in DED processes induces a large value of residual stresses. These residual stresses are developed from the reiteration of heating/cooling cycles and from the high temperature gradient that occurs during the process. Moreover, the thermal misfit between two adjacent regions was observed to highly influence the residual stresses in DED-based processes [37]. To understand the effect of build strategy on the residual stress of 316L specimens, Saboori et al. fabricated two cubes with 90° and 67° scan rotation angles [38]. For the cubes built with 90° rotation, a difference on the stress distributions is observed at a depth of approximately 0.4 mm, where the maximum stress of the sample was up to 200 MPa. Comparing the direction of principal stress, it is possible to observe that the angle is positive for more than half of the analyzed depth. Notably, the maximum stress is obtained at a depth of approximately 0.4 mm, and after a depth of 0.6 mm, the stresses become almost constant. For the cube fabricated using 67° scan rotation, the residual stresses

exhibit an oscillatory trend. For these cubes, the maximum value of stress is approximately 150 MPa. Table 2.2 summarizes the measurements of residual stresses on the analyzed cubes [38]. Comparing the value of residual stresses, lower residual stresses can be obtained using a 67° scanning strategy. Moreover, it is possible to state that the residual stresses on top surfaces, in both cases, are lower compared with residual stresses obtained on lateral surfaces. This behavior was attributed to the different cooling rate deriving from the different deposition pattern used in the experimental tests. In particular, higher residual stresses were characteristic of higher cooling rate.

Table 2.2. Overview of residual stress measurements in DED 316L cubes [38].

Cube	Principal stress component	Stress (MPa)					
		Top		Side A		Side B	
		Min.	Max.	Min.	Max.	Min.	Max.
C-0090-1	σ_{max}	−77	233	−50	635	−160	376
	σ_{min}	−164	165	−211	119	−243	165
C-0090-2	σ_{max}	−164	181	−97	442	−104	341
	σ_{min}	−173	169	−138	253	−140	194
C-0067-1	σ_{max}	−172	133	61	265	−179	278
	σ_{min}	−204	103	−139	118	−302	134
C-0067-2	σ_{max}	−40	142	−146	240	−110	312
	σ_{min}	−92	71	−286	101	−114	291

2.3.2 Mechanical Properties of Directed Energy Deposition 316L

The hardness of the sample made from the middle of a WAAM 316L part was measured in the build direction [39]. According to the observations, the hardness of the WAAM 316L was homogeneous with an average hardness of approximately 192.1 HV (Vickers pyramid number). As compiled in Table 2.3, corresponding tensile tests performed on the same samples showed that the tensile strength in the BD is approximately 50 MPa (8.8%) lower compared with the tensile strength measured in the DD. The maximum tensile strength was 577 MPa in the DD. The yield strength was approximately 30 MPa lower in the BD. However, the elongation in the BD was 6.6% higher.

Table 2.3. Compilation of tensile strength in WAAM 316L.

Material	BD	DD
Yield strength (MPa)	302 ± 9.3	333 ± 15.8
Tensile strength (MPa)	526 ± 3.4	577 ±5.5
Elongation (%)	34.9 ± 0.5	28.3 ± 0.9

To investigate the mechanical behavior of the laser DED 316L SS sample, Van Nuland et al. conducted tensile tests on dog bone specimens obtained from the sample [35, 40]. In each plane, three different tensile loading directions were tested: horizontal direction (TD or DD), vertical direction (BD), and diagonal direction (45°), with multiple specimens per loading direction. The measured stress–strain responses are visualized in Figure 2.10(a) and Figure 2.10(b) for the dog bone specimens in the TD–BD and DD–BD planes, respectively. In the TD–BD plane [Figure 2.10(a)], they observed a clear anisotropic response, with a higher initial yield stress obtained in the transverse direction, compared with the building and diagonal loading directions. In comparison, for the DD–BD plane [Figure 2.10(b)], the lowest yield stress is found in the BD. In this plane, the variations in stress level obtained from multiple specimens in the same loading direction are much larger than the stress variations observed in the TD–BD plane. The speculation was that

for the DD–BD specimens, the 2 mm thickness (in the TD) is smaller than the average size of a fusion zone in the TD of 5.41 mm, causing only a part of the entire fusion zone texture to be tested in each of the experimental measurements in the DD–BD plane. For loading in the TD and diagonal direction (TD–BD), a very inhomogeneous deformation pattern is observed. In the TD, multiple localizations occur in the overlapping regions of the fusion zones. For loading in the diagonal direction (TD–BD), these localizations appeared at the center of the fusion zones. For loading in the BD, a more homogeneous deformation is observed, with only a single neck at large strain. These deformation patterns directly result from the underlying WAAM microstructure.

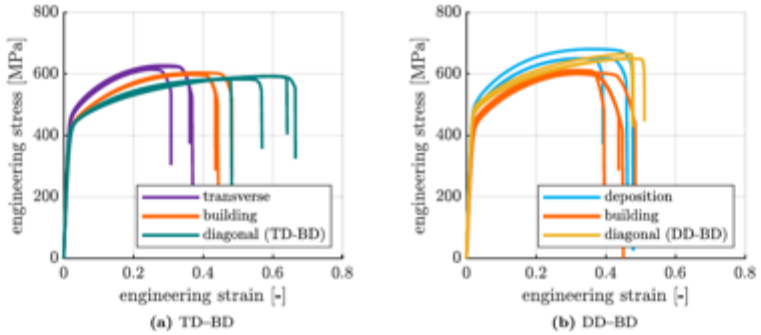

Figure 2.10. Tensile property response of WAAM 316L SS for dog bone specimens in the cross-sectional planes (a) TD–BD and (b) DD–BD [40].

3. LARGE-SCALE ADDITIVE MANUFACTURING MODALITIES

3.1 LARGE-SCALE ADDITIVE MANUFACTURING: WIRE VS. BLOWN POWDER DIRECTED ENERGY DEPOSITION PROCESS

DED is an efficient and effective technology for adding material on the surface of existing parts. Compared with conventional casting, the DED technique reduces initial investment by not requiring casting molds. Additionally, DED offers near net shape structures, which significantly reduce machining and material waste compared with forging. High-speed printing via DED can also enable printing of large-scale structures at a high production rate. As with all AM-based, system-level fabrication tools, DED allows for the creation of objects in a layer-by-layer fashion by melting material (most frequently used for metals such as titanium, aluminum, SS, or copper) in powder or wire form with a focused energy source [41].

In the AM industry, wire arc AM (WAAM) and laser wire-feed AM (LWAM) are both forms of AM that use wire as a material feedstock. The main difference is the type of energy used to melt the wire. WAAM uses an electric arc, and LWAM uses a laser source. WAAM tends to be faster and more efficient than LWAM, but the latter produces parts with higher precision and surface quality. The operating windows of WAAM and LWAM can be complementary and alternative. Usually, WAAM can provide a high deposition rate, and LWAM enables sufficient control to build medium to small features with near net shape characteristics. Figure 3.1 provides a schematic of WAAM equipment and an illustration of its installation [42–44]. Because of the process's high speed and environmental cooling, some defects are created in the additive samples [45]. However, AM parts with increased weight and volume have unique disadvantages, such as cracks and microcracks, incomplete process, porosity, and lack of adhesion of printed layers, which can be addressed by controlling and optimizing the hardware inputs and relevant parameters [46–48].

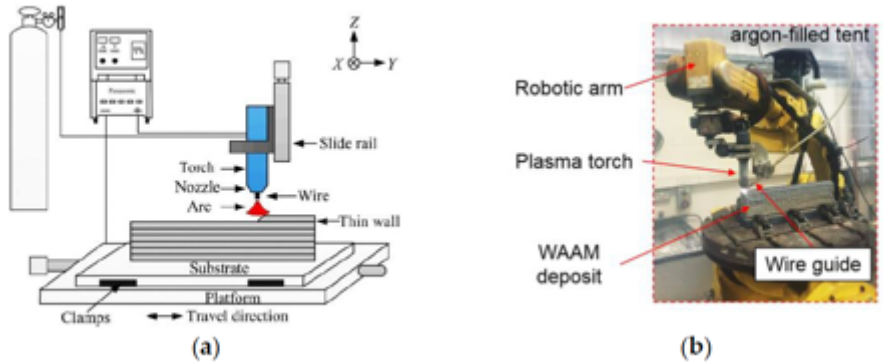

Figure 3.1. Installation and schema of WAAM processes (a) schematic and (b) WAAM equipment [43, 44].

In the LWAM technique, the metal wires are melted with a laser beam and deposited in a line shape to create a sample with a complex geometry design (Figure 3.2) [49]. The patterns in this technique and the input laser parameters significantly influence the quality of the AM samples. In the LWAM process, the solidification rate in the melt pool is linked to laser speed and power. Thus, optimizing the LWAM parameters can reduce the level of porosity [50]. Sometimes in this technique, the environment air or shielding gases are trapped inside the AM structures, and a range of porosities may appear in the AM samples.

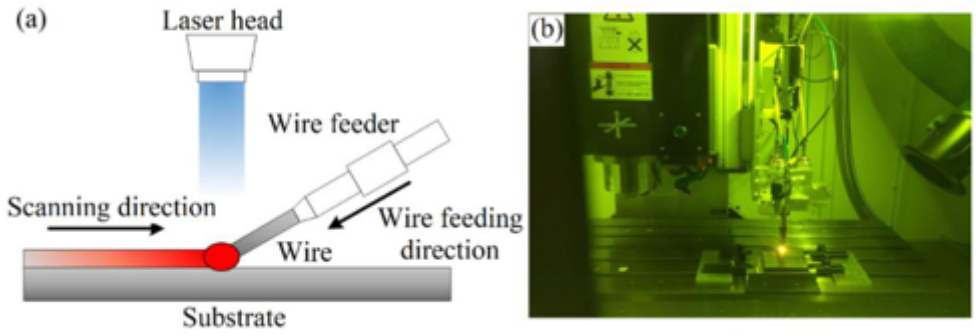

Figure 3.2. Installation and schema of LWAM processes (a) schematic and (b) LWAM. equipment.[49]

In the case of a BP-DED system, a heat source (laser, electron beam, or plasma) is used to focus on the substrate to create a melt pool into which the powder feedstock is delivered via an inert gas flowing through a multinozzle assembly (Figure 3.3) [51]. The nozzle is designed such that the powder streams converge at the same point on the focused laser beam. Subsequently, the substrate is moved relative to the laser beam on a computer-controlled stage to deposit thin layers of controlled width and thickness. DED machines often have inert gas blown together with the powder from the nozzles or the availability of shield gas during deposition, thereby sheathing the melted region and reducing the oxidization rate. For systems that are enclosed in a glove box, the oxygen content can be maintained below 10 ppm during all deposition conditions.

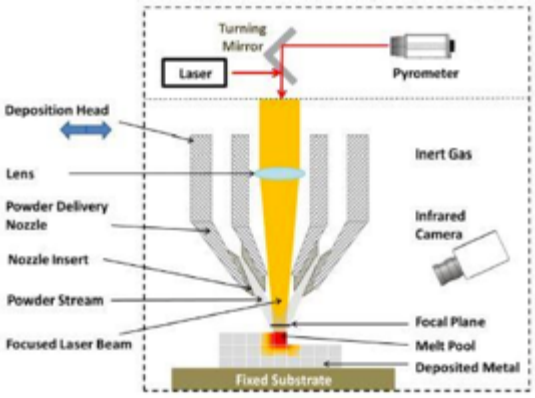

Figure 3.3. Schematic of BP-DED modality with thermal monitoring [51].

3.2 WIRE ARC ADDITIVE MANUFACTURING

3.2.1 Wire Arc Additive Manufacturing Machine

WAAM is a wire-feed AM process and one of the most promising techniques for producing larger components with moderate complexity and relative low costs compared with other AM techniques for metals [52]. WAAM processes have a promising future. Designs are already being made using this technique in different fields, and WAAM is performing very well; some of these fields include lightweight aerospace components (landing gear parts, wing ribs or stiffeners) [53], wind tunnel models [54], bridges [55], and complex constructive features (such as the dragon bench in the manufacture of furniture) that could not be made with conventional processes such as casting or computer numerical controlled milling, among others [56].

WAAM processes generally involve high residual stresses owing to high deposition rates and heat inputs [57]. The influences of process conditions (for example, energy input, wire-feed rate [58], welding speed, and deposition pattern) on thermal history, microstructure, and resultant mechanical and surface properties of parts need to be analyzed because not enough knowledge exists in the scientific community yet [59].

3.2.2 Pressure Vessel Fabrication Using Wire Arc Additive Manufacturing

Arc-based wire-feed metal AM was chosen as the best process to produce large metal parts [60]. Although metal powder bed printers are available commercially, they are not currently capable of producing large-scale metal parts [61]. Welding-based systems are not as precise as powder bed systems in terms of print resolution, but there are no inherent limitations to print reasonably sized parts. Postprocess machining of either print technology is typically required for the final product. Therefore, arc-based wire-feed technology provided the most cost-effective solution. GMAW was used to build a pressure vessel (e.g. a HIP can) using Lincoln Electric Power Wave Technology tuned for low heat input deposition, which allows metal deposits to be stacked in an environment of argon and CO_2 at the ratio of 96%:4% [62]. A 0.045 in. diameter (ER70S6) [63] 70 ksi low-carbon steel wire was used for the feedstock, which provided sufficient deposition fluidity/wetting and mechanical properties. The system was built with a Lincoln Power Wave S500 welder and AutoDrive SA servo wire feeder with a secondary push-pull servo motor at the deposition head. This type of wire feeder allows for adequate control of the length of the wire between the surface of the part and the tip of the torch throughout hours of printing. The system was equipped with an arc tracking system, which measured the impedance of the welding arc and provided corrections to maintain a specified current [62]. The use of the arc tracking system resulted in consistent contact between the welding tip and the component being fabricated. It also allowed for automated control of the distance of the torch over the part and prevention of part torch collision. Additionally, another closed loop control system was developed and implemented to control the build height of the part. This way, the robotic arm was automatically correcting the build height of the part and overriding the command coming from the slicer-generated G-Code commands.

One of the characteristic features of DED metal AM is its variability, especially in the *z* direction. Vertical growth of a part heavily depends on the geometry of the part, environmental conditions of build area, and process settings of the AM system. A variable geometry and an open chamber with an ambient environment cause fluctuation in layer height. On the other hand, the GMAW process depends on proper wire-to-part contact. Proper arc starts are important for limiting deposition voids.

A constant distance between the bead and the electrode is also important for high quality builds. In standard, open-loop processes, the head's *z* height is preprogrammed. Even with excellent proper starts and height tracing, final part shape is not guaranteed. Although the process is stable and the material quality is high, the *z* (vertical) geometrical tolerances are not guaranteed without minimizing the absolute *z* height error [64]. The *z* build errors tend to accumulate from layer to layer, resulting in eventual catastrophic failures. For example, build corner features tend to overbuild, and overhang features tend to underbuild. The implemented solution is a closed-loop control system that automatically adjusts the amount of material deposited [64]. This adjustment results in long-term geometrical accuracy and limits the number of print faults.

In the beginning, a simpler concentric cylinder with 60° inward and outward inclined walls were built (build can A). The successful open structure build provided an opportunity to assess the build quality (Figure 3.4). Figure 3.5 shows top, side, and isometric views of the preliminary part. Notably, after the completion of the bottom outer inclined section, the weld mode needed to be tuned to enable a relatively smooth vertical wall build.

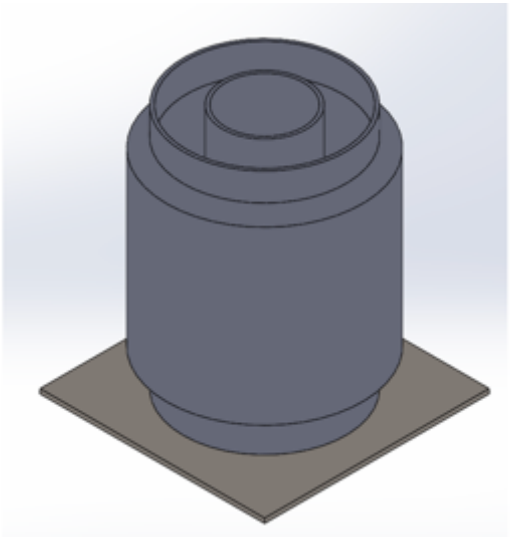

Figure 3.4. Preliminary CAD model of simpler concentric thin-wall build with 60° inward and outward inclined walls.

Figure 3.5. Top, side, and isometric views of build can A.

The follow-up build (build can B) had a much taller wall height, along with an added lip that was built on the top surface. This structure enabled a subsequent addition and welding of sheet metal on top of the two concentric thin wall builds. It also ensured a tight seal around a hollow, enclosed volume, as shown in Figure 3.6.

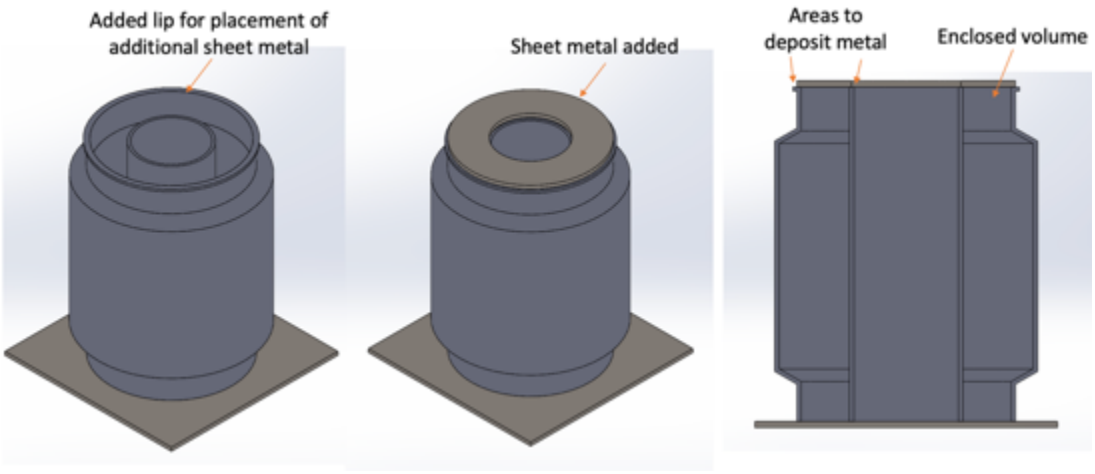

Figure 3.6. Sequential steps, as shown using a CAD model, to generate an enclosed volume within two concentric thin walls for build can B.

The final WAAM builds from above two iterations are shown in Figure 3.7. The corresponding Table 3.1 is a compilation of build dimensions that includes height, outer diameter (OD), and inner diameter (ID). Notably, out of the two build cans, only can B has a completely sealed enclosure because of a welded plate on the top, along with a weld tube. Can B is currently being evaluated and prepped to undergo conventional HIP cycles.

Figure 3.7. Side views of build cans A and B. Can B has a welded plate on the top, along with a weld tube.

Table 3.1. Compilation of final dimensions of build cans A and B.

Property	Can A	Can B
Height (in.)	7.75	13.5
OD max (in.)	10	10
ID min. (in.)	7.75	4.0
Termination	None	1/4 in. annular plate

3.3 HYBRID ADDITIVE MANUFACTURING

3.3.1 Hybrid Additive Manufacturing Machines

The first iteration of the pressure vessel was built on Mazak VC-500 using 316LSi SS wire. This is an off-axis deposition system and was primarily used for process parameter development. No in situ data were captured, and no weld pool camera was associated with the data. This tool presented challenges around off-axis welding. At times, welding without dwell times between layers led to excess heat in the thin walls, which led to drooping. Constant human monitoring was needed to diagnose layer height issues, weld wires, and thermal inconsistencies. The manufacturing of a more successful HIP valve was done in a hybrid machine tool as depicted in Figure 3.8. The VTC-800G SR AM is a multiaxis machining and laser hot-wire additive system from Mazak. Machine capabilities include a six-axis machining center, as well as five axes of deposition in a large platform, with a maximum work piece volume of 1.5 m in height by 0.75 m in diameter. The maximum additive specifications include an 8 kW single-beam laser split into a tribeam that converges on the weld pool, with an additional 1 kW of hot-wire power available. Hybrid machine tools allow for the manufacturing of a multitude of industrial applications while reducing the amount of waste, feedstock, and time required to make components. In the case of the HIP component, a similar theory was applied.

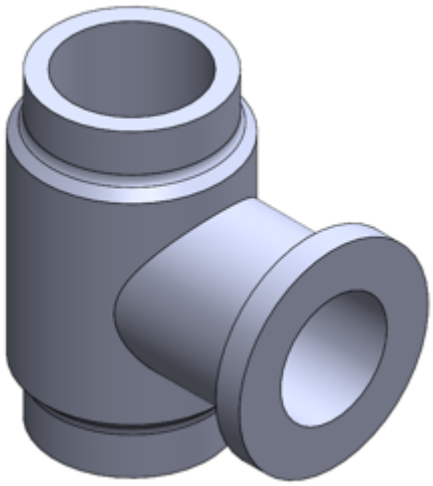

Figure 3.8. HIP valve geometry shown in isometric view.

3.3.2 Pressure Vessel Fabrication using Hybrid Additive Manufacturing

Large castings and forgings typically take months to make, with additional months needed to modify if a casting is insufficient or lacks features. A proposed solution is the use of AM. AM is used to create a shell of a traditionally forged component, which can then be filled with a filler powder to undergo the HIP process. Through this process, the replacement part would contain very few defects, be economical, and

have well-understood material properties. HIP with a hybrid manufacturing system allows for greater complexity of a single component within one machine platform. Additionally, doing the manufacturing with a hybrid manufacturing platform allows for the component to be reoriented in the machine for ease of accessibility. The HIP valve detailed in this report is a single wall bead thickness of approximately 7 mm while being entirely hollow and enclosed. The internal cross-sectional view is shown in Figure 3.9.

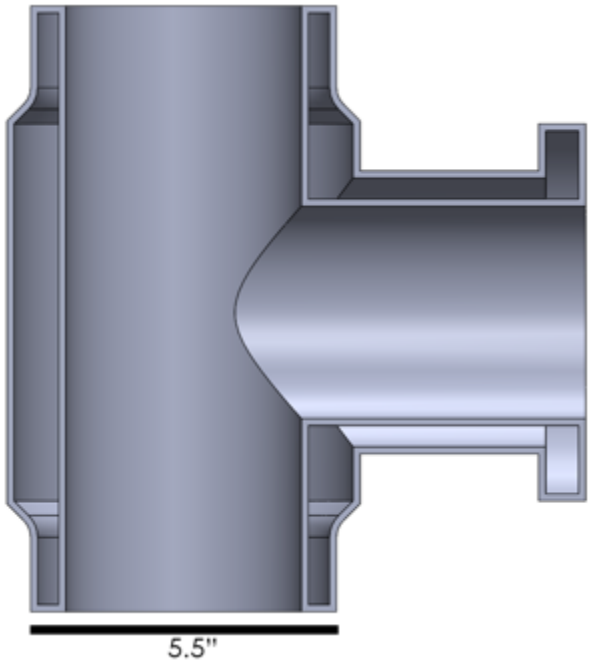

Figure 3.9. HIP valve geometry with cross section view.

A challenge by the DED industry has been manufacturing fully enclosed hollow structures; typically machine limits and tool pathing are challenges to overcome. A common alternative strategy is to curve edges and print nonright angles to account for overhangs. The part detailed in this report was completed with full right-angle overhangs within one machine tool and is fully enclosed. The creation of this part was enabled by a method developed through using distinct stepovers, print angles, and process parameters. With these new methods, challenges arose, which required additional steps to mitigate.

First, the HIP valve must be deconstructed into basic forms, which ultimately consists of cylinders. For the major cylinder, traditional AM would require complex deposition angles or support structures to form the hole subsection in the part. As a result of having subtractive capabilities, the major cylinder was programmed as a solid tube with no hole, then subsequently programmed to have the cutout section machined. As shown in Figure 3.10, the major cylinder changed for the programming setup.

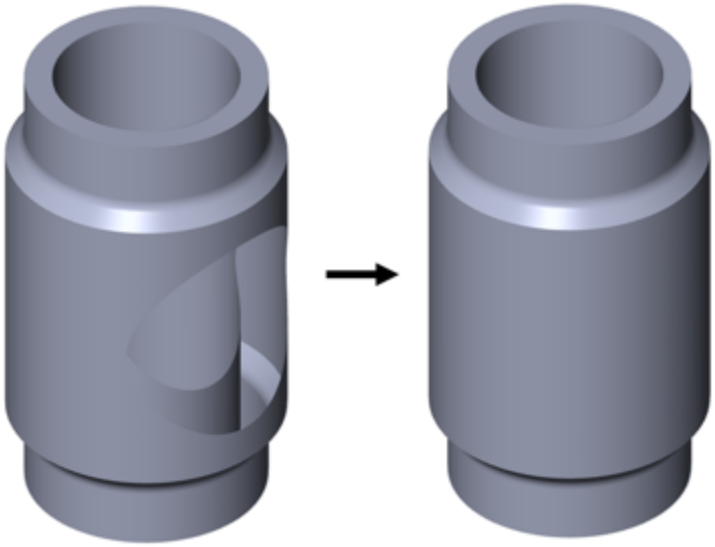

Figure 3.10. Major cylinder of HIP valve (left) before and (right) after geometry adjustment.

Once an initial parameter set was chosen based on previous build settings, new toolpaths were made to account for the limited standoff height for the welding nozzle. At a maximum of approximately 10 mm standoff, the layer height and angles of deposition had to be carefully monitored to prevent machine issues. The VTC-800G SR AM has a traditional *xyz* coordinate system, as well as two rotational axes designated *A* and *C*. Rotational axes allow for consistent printing of cylindrical features; as a result, concentric ring paths in the vertical orientation were preferred. The major cylinder was setup such that the offshoot cylinder can be prepared in the same orientation. The printing took approximately 7 h, with the result shown in Figure 3.11. The challenges faced related to the toolpath of keeping the deposition head perpendicular to the printed surface. The outer wall flanges are 45°, which prompted some unique solutions. As opposed to a continuous build, the inner and outer walls at the angled flanges were printed in alternating paths as opposed to printed simultaneously. The straight wall sections were all completed in as few toolpaths as possible while being printed in a simultaneous motion. Ultimately, no major challenges were posed by the completion of the major cylinder. The top lid face, as depicted in Figure 3.12, was completed using a unique stepover, layer height, and toolpath compared with the typical parameters.

Figure 3.11. Major cylinder after printing shown in the vertical orientation.

Figure 3.12. The top lid of the major cylinder section printed as a 90° overhang.

The overhang strategy was done with a specific deposition angle and yielded ideal results. The final top lid produced a sharp print, as well as a fully enclosed the hollow tube. An identical strategy was developed for the remaining 90° overhangs. Initial machining will allow for a smooth deposition surface and ease of reach during further toolpaths. As a result, the full outside surface of the major cylinder was machined to a net shape (Figure 3.13).

The prep for the offshoot cylinder involves printing a cylindrical section opposite the hole side. This is owing to the machine kinematics of any standard five-axis machine tool not being able to support all motions required to print the HIP can in concentric rings. The issue is further detailed in Figure 3.14 and Figure 3.15, which depict the standard kinematic configuration for printing the major cylinder, along with the refixturing setup for further printing. This fixturing setup is entirely made as sacrificial material, and using DED enables minimal waste by only printing the features that are needed.

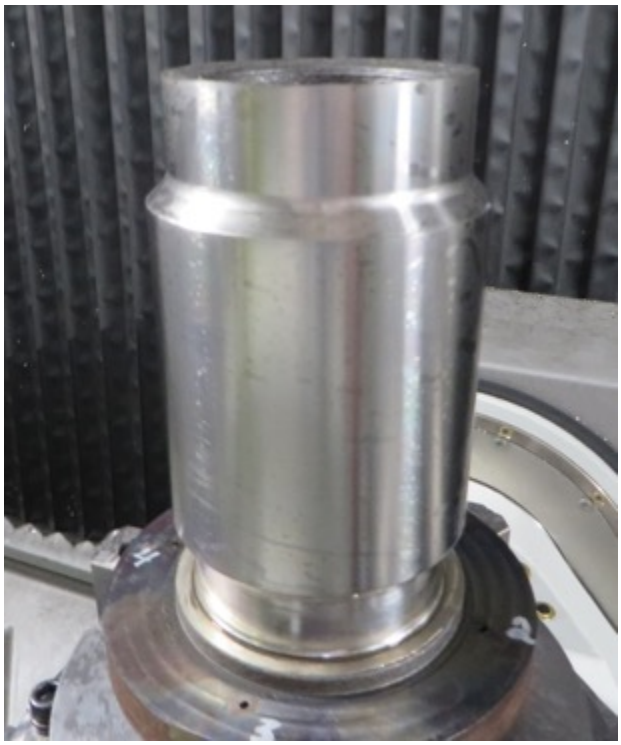

Figure 3.13. The final machined major cylinder.

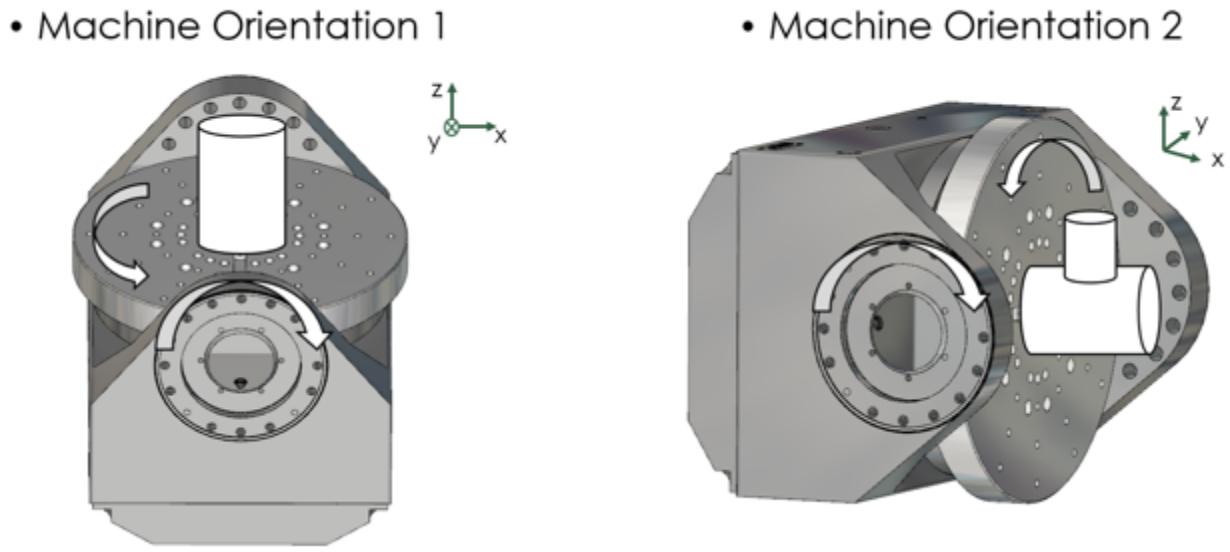

Figure 3.14. Initial orientation allows for (left) major and (right) offshoot cylinder to be printed as shown.

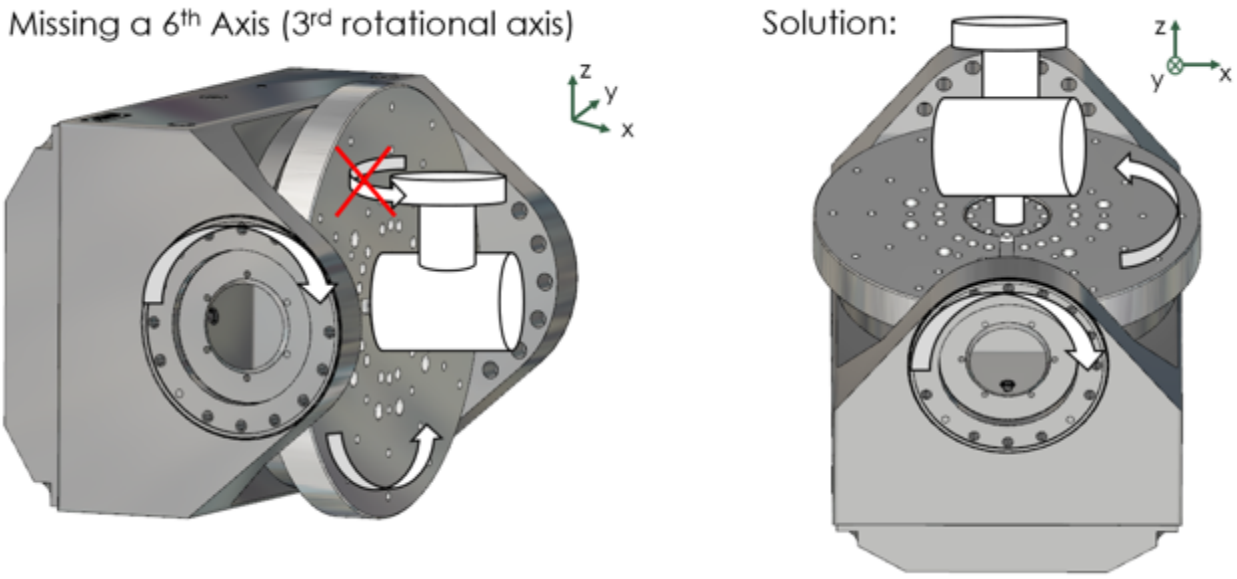

Figure 3.15. The (left) cylindrical flange and (right) solution with printed fixture.

The cylindrical flange cannot be printed concentric to a rotational axis in standard machine configuration. As a result, the printed fixture point is completed through DED and machining to reorient the part, as shown in Figure 3.16 and Figure 3.17, respectively.

Figure 3.16. The DED fixturing tube shown on the major cylinder.

Figure 3.17. The machined fixturing tube prepared for refixturing.

With the refixturing tube prepared with machining, the HIP can is reoriented in the machine in a horizontal position, as shown in Figure 3.18. The next step will be machining a hole through the outer wall of the HIP can such that deposition can occur on the inner wall. This step is vital in forming a 90° angled hollow section internally. The deposition angle is vital in preventing the additive head from colliding with the outer machined wall. The initial inner wall deposition is shown in Figure 3.19.

Figure 3.18. The machined outer wall prepared for offshoot printing.

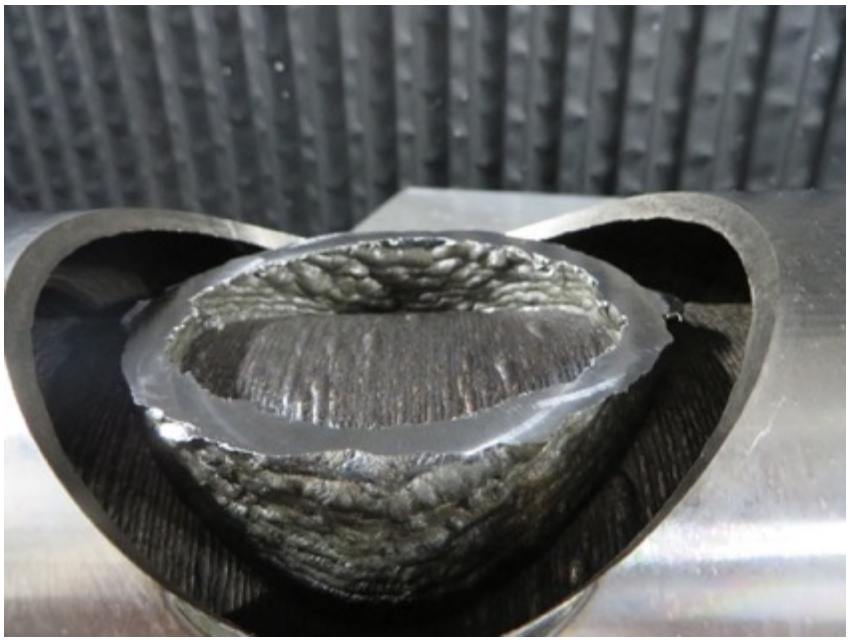

Figure 3.19. The inner printed wall that forms a 90° bend in the internal cavity.

With the internal section print begun, the outer rim of the hole was printed along using contour paths to form the outer wall of the offshoot tube. Figure 3.20 showcases the difference in strategies between the inner and outer wall prints, with the outer wall contour matching the curve of the major cylinder. The inner wall was printed using vertical concentric rings.

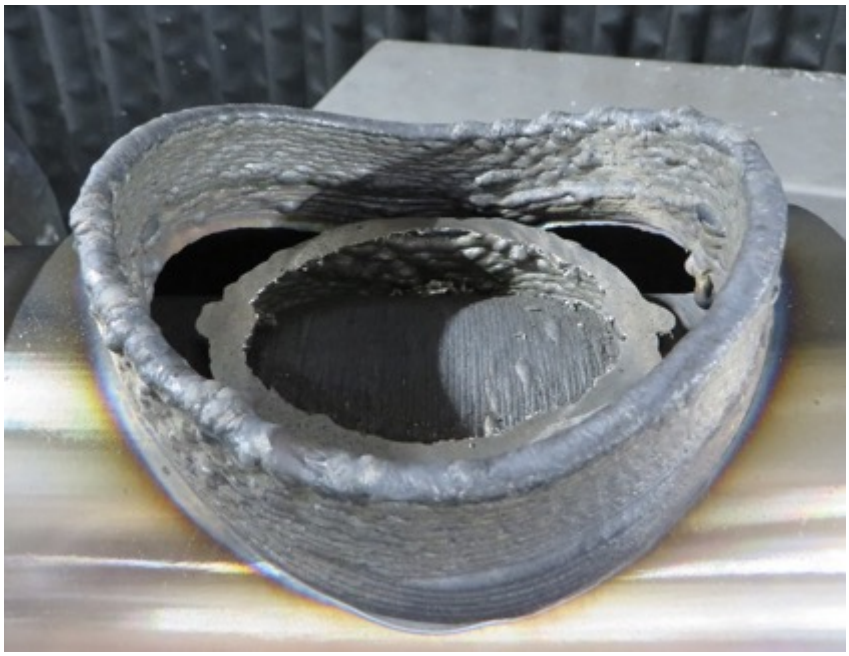

Figure 3.20. The inner and outer walls of the offshoot tube after printing and machining.

Once the offshoot tube was printed to net height, a gap was left between inner and outer wall thicknesses to allow for printing the outer flange (Figure 3.21). In Figure 3.22, the starting steps of the outer flange print are shown. Additionally, the deposition angle for straight 90° overhangs was not done at a

perpendicular angle; this choice was a result of not only machine limitations but also layer height accommodation for thin wall heat distribution. Excessive heat directionally distributed into the part can have adverse effects on overall shape. As a result, an off-axis deposition angle was used, as shown in Figure 3.23.

Figure 3.21. The expanded printing of the offshoot tube.

Figure 3.22. Outer flange deposition on flat surface.

Figure 3.23. Off-axis deposition angle for flange.

With the flange walls printed, the final build section was to close the thin-walled section by enclosing the hollow space. In DED, this process is seen as a difficult challenge, which can be attributed to the accessibility, geometry, and printing parameter constraints of any given machine. In this machine, printing was successfully completed off-axis in a similar strategy to the previously discussed strategy for enclosing the top lid of the major cylinder. The result is shown in Figure 3.24. A large success is attributed to the benefit of making a fully enclosed structure (10.5 in. tall and 5.5 in. OD) that has sharp, 90° angles printed with no support structures. The part is currently being evaluated and prepped to undergo conventional HIP cycles.

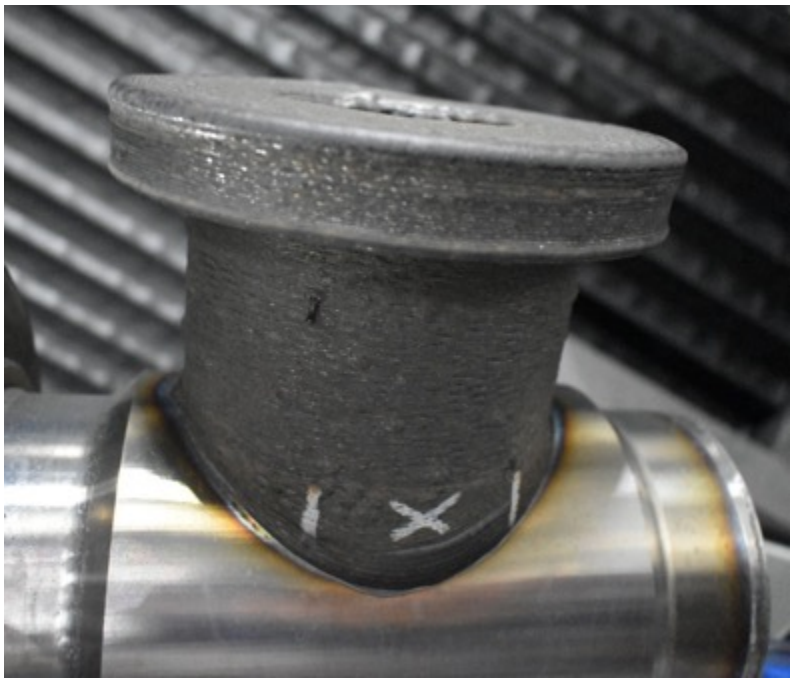

Figure 3.24. The fully enclosed HIP Can flange.

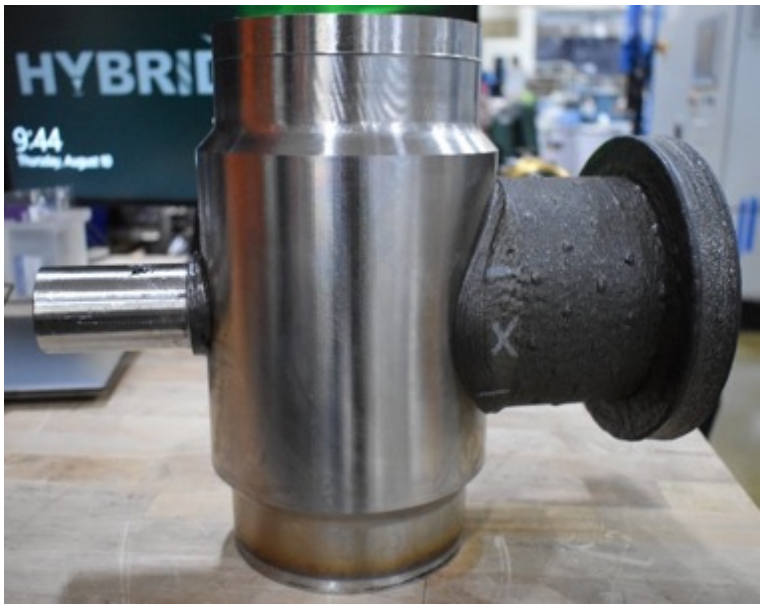

Figure 3.25. The final HIP can after machining away the substrate.

3.4 BLOWN POWDER DIRECTED ENERGY DEPOSITION ADDITIVE MANUFACTURING

3.4.1 Blown Powder Directed Energy Deposition Machine

The AddUp BeAM Modulo 400 is a blown powder laser DED AM tool with a working volume of 650 × 400 × 400 mm (see Figure 3.26). This five-axis machine is capable of depositing weld beads approximately 1.0 mm wide in an inert environment from a feedstock of powder that can be simultaneously delivered from one to three powder hoppers. The machine is equipped with two nozzles of different sizes and power. The 10Vx deposition nozzle can deposit weld beads 0.8 to 1.2 mm wide, with an accuracy of 0.1 mm. The 24Vx deposition nozzle can deposit weld beads 2 to 2.4 mm wide, with an accuracy of 0.2 mm. The Modulo 400 machine is also equipped with an enclosure inert device, which allows working with reactive powders [65].

Figure 3.26. Image of the AddUp BeAM Modulo 400 Laser DED AM machine. Powder flow from three of the five powder hoppers on the right of the image can be used and controlled simultaneously and independently during printing.

3.4.2 Pressure Vessel Fabrication using Blown Powder Directed Energy Deposition

Efforts to explore technologies to fabricate HIP cans for large-scale applications have also been extended to blown powder DED. The initial focus of DED HIP can fabrication was to determine the vacuum integrity of a large-area, thin-walled closed structure. Figure 3.27(a) shows the six-chamber DED 316L SS structure chosen for evaluation. It has an overall height of 250 mm and an OD ranging from 120 mm at its base to 250 mm at its top. The wall thickness is approximately 2.4 mm and was created using two laser passes (two laser beads). The outer and inner walls of each chamber are separated by approximately 12 mm. Because of challenges associated with printing overhanging beads, each chamber was initially printed without a top. Tops were then fabricated from a rolled 316L SS plate using wire electrical discharge machining and welded to the chamber walls using the DED machine.

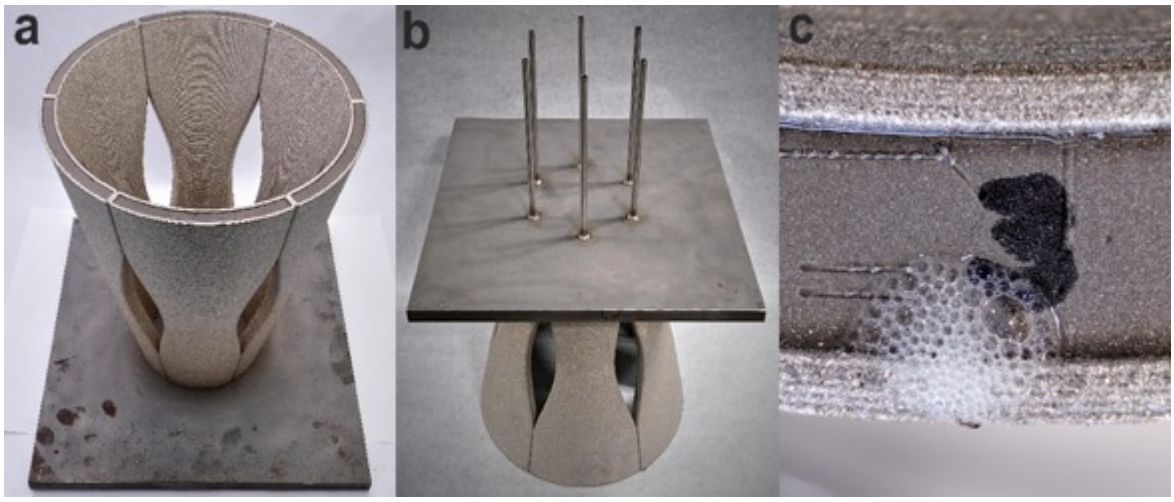

Figure 3.27. Six-chamber 316L SS DED HIP structure: (a) top view showing welded top plates, (b) bottom view showing six tubes for powder filling and pressure testing, and (c) soap bubble leak observed during pressure testing.

For pressure testing and filling with powder, six holes were drilled through the substrate, and tubes were welded into the holes [Figure 3.27(b)]. When 15 psig of air pressure was applied to each chamber, leaks were observed in five of the six chambers [Figure 3.27(c)]. In all cases, leaks were only observed at the junction of the chamber wall and the rolled top plate. No leaks were observed through the walls of the chambers nor at the junctions of the walls and the substrate.

These preliminary results suggest that (1) two-bead, approximately 2.4 mm thick DED walls are likely sufficient for fabricating HIP cans and (2) the joining of DED walls to a rolled plate using DED welding may be challenging and require further development. Efforts are underway to design and demonstrate DED HIP cans that do not require closure plates. Figure 3.28 shows examples of potential closed HIP can designs with varying complexity. The demonstration of such designs will likely require the use of five-axis printing on the BeAM printer. This five-axis printing capability is currently under development at the Oak Ridge National Laboratory Manufacturing Demonstration Facility.

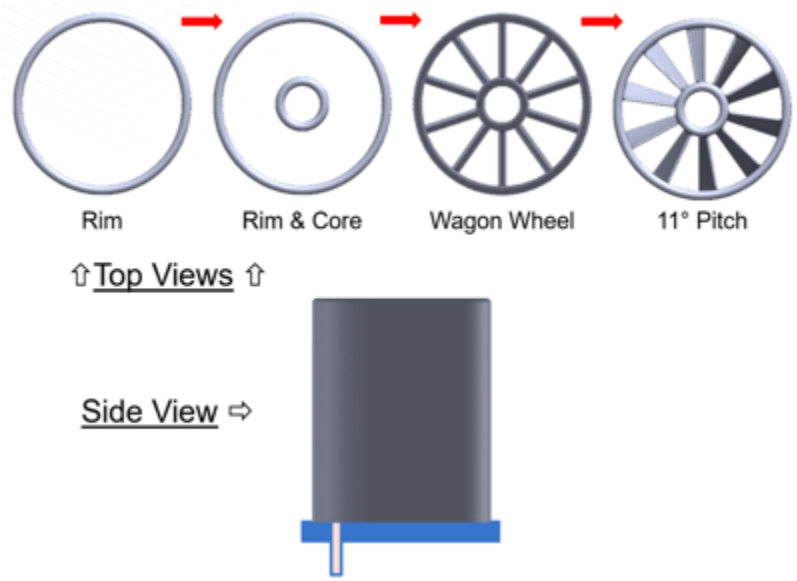

Figure 3.28. Designs for closed HIP cans showing varying degrees of complexity.

4. IN SITU MONITORING TECHNIQUES FOR DIRECTED ENERGY DEPOSITION

4.1 IN SITU MONITORING NEEDS

Accreditation of additively manufactured parts is critical for AM's broad adoption and acceptance in the industrial sectors. The AM product qualification timeline comprises design engineering and supply chain substantiation and development, but the longest task in the timeline is process authentication. On top of that time, the AM process is highly dependent on build parameters, machine-to-machine variability, or even process control variations owing to changes in environmental conditions [66]. The complex interplay between process variables and final parts can be roughly depicted by Figure 4.1 [67].

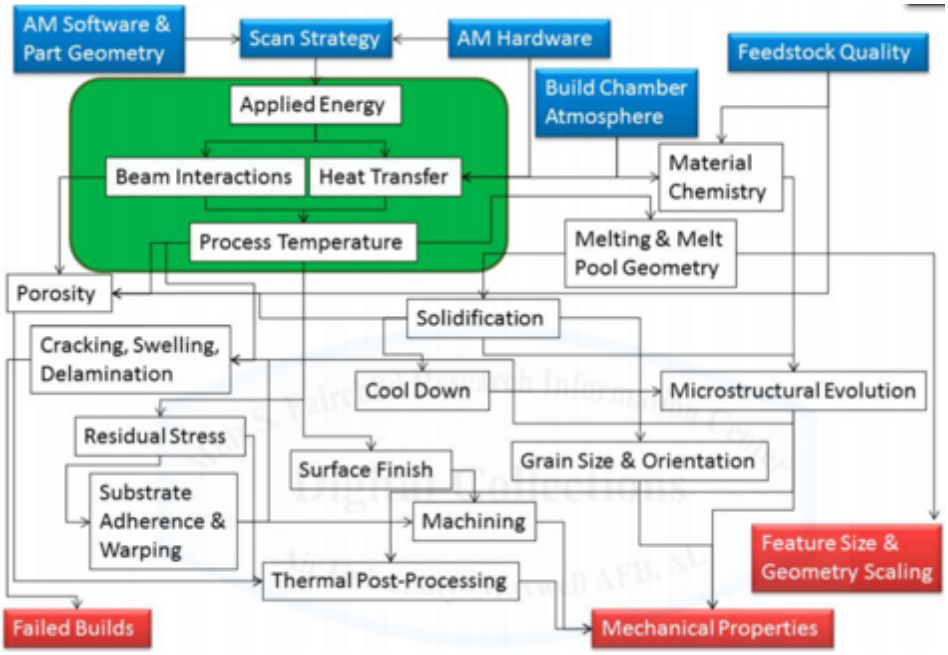

Figure 4.1. Process map showing interrelations between process variables and final part [67].

To guarantee a product that is not defect limited, manufacturers currently integrate process monitoring and control during part manufacturing. Unlike conventional metal fabrication and cutting processes, where in-process gauging and adaptive control are well-established, such technologies in the AM process are still growing [68]. New monitoring techniques and associated control strategies are in play, mostly to enhance product quality and confidence around part performance. Melt pool and thermal monitoring and defect and distortion identification during the AM process are emerging areas of research. Several approaches can tackle this problem, some being computer vision, acoustics, and spectroscopy. Specifically for DED, which is a multipass welding process, the build process can be quite complicated with nonuniform heating and cooling cycles, depending on the choice of scanning strategy [69]. Thermal transfer in DED has been shown to be highly dependent on geometry and has many important consequences on process stability [70], microstructure [71], and mechanical properties [72]. One particular concern is the introduction of residual stresses and distortion from thermal expansion [73], which in many material systems induces cracking [74], substantial work, and dislocation generation [75], as well as a general inability to meet dimensional tolerances without postmachining. The severe consequences of this thermal nonuniformity have motivated a broad field of monitoring and control research to improve the capabilities of the process [76]. These capabilities can be divided into four categories: (1) point measurements such as thermocouples or strain gauges, (2) integrated measurements such as acoustic or photonic emission monitoring, (3) local melt pool

measurements such as coaxial thermal and multispectral imaging, and (4) global measurements such as a thermal camera viewing the entire part [77–80].

4.2 IN SITU MONITORING CAPABILITIES IN WIRE ARC ADDITIVE MANUFACTURING MACHINE

Build data for the Arc 1 cell were acquired using a National Instruments CompactRIO controller. This controller runs LabVIEW code on the LinuxRT operating system, allowing it to operate independently of the host PC (Figure 4.2). A user interface, also created using LabVIEW, is run on the host, allowing the user to view and interact with the data. Data collected include weld data such as current, voltage, and wire feed info received directly from the welders; data on the status of the robot, including position, move speed, and info on the current task; thermal data from infrared (IR) cameras; and efficiency data based on the uptime vs. downtime of the robot. Additionally, the system can also be used to automatically manage the interpass temperature of the part by feeding thermal data to the robot between layers. IR images and video can be saved automatically in each layer or manually as desired by the user. All other data are recorded as text. Data is collected at a rate of 10 Hz. The software and hardware are modular, making them easy to reconfigure to add or remove data sources as needed.

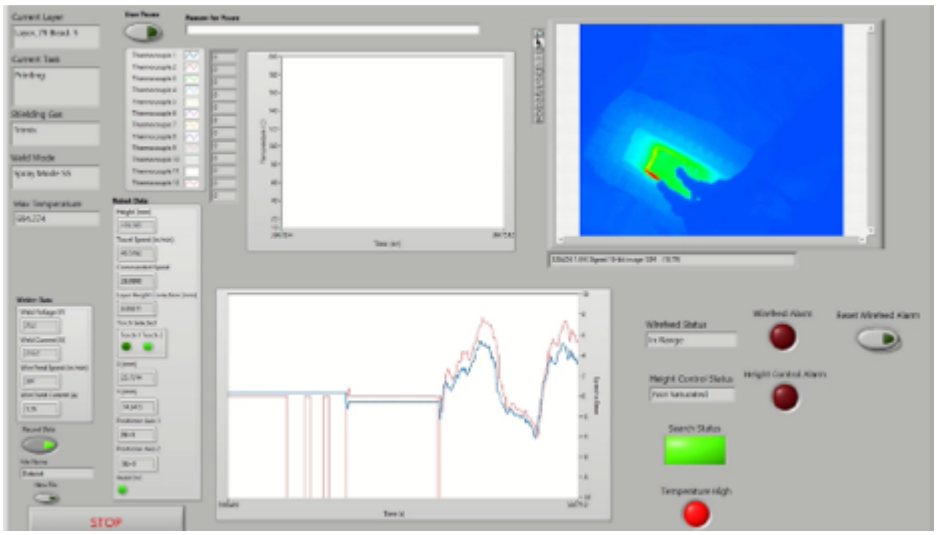

Figure 4.2. A typical LabVIEW output capturing various thermal data acquired during the WAAM process.

4.3 IN SITU MONITORING CAPABILITIES IN HYBRID ADDITIVE MANUFACTURING MACHINE

For thermal imaging, long-wave (8–14 µm), midwave (0.9–1.7 µm) or near-IR (0.75–1.4 µm) may be used [81]. The goal is to measure approximate temperature and temperature distribution when building a part. The off-axis IR camera can be used to obtain thermal history of a part, along with thermal gradients and melt pool–related data [82]. Hyperspectral imaging may be used to extract accurate temperature data from laser welding without prior knowledge of emissivity [83].

Another important aspect for defect detection in hybrid manufacturing is the ability to employ vision-based melt pool monitoring and real-time melt pool size measurement [81]. In situ melt pool dynamics in AM can be measured either by off-axis or on-axis energy sources to gather a variety of signals for imaging, thermography, spectroscopy, and topographic evaluation [81, 84–86].

The deployment of K-Type thermocouples is convenient during the DED AM process, and the acquired data are essential for the development of 2D temperature evolution models. These data can also be used as references to set the duration of 2D thermal simulations, including actual information on the average heating and cooling periods (defining a numerical idle time) [87]. They undergo a deviation in output when magnetic material reaches its Curie point at around 185°C. Also, K-Type thermocouples work very well in oxidizing atmospheres at temperatures up to 1,260°C (2,300°F), and their tolerance class is ±1.5 K between −40°C and 375°C.

In the current setup, a total of two Axis video cameras, one off-axis forward-looking IR (FLIR) thermal camera, a Xiris WeldStudio camera for weld pool monitoring, and a Madgetech data logger monitoring system with four standard K-Type thermocouples (one in each quadrant) were used to gather in situ process monitoring data during the entire build process. The visual and FLIR camera setup are shown in Figure 4.3, and the thermocouple setup is shown in Figure 4.4. This setup allowed for a full suite of visual, thermal, and weld pool monitoring in process. Data were captured at a rate of approximately 25 gigabits/min.

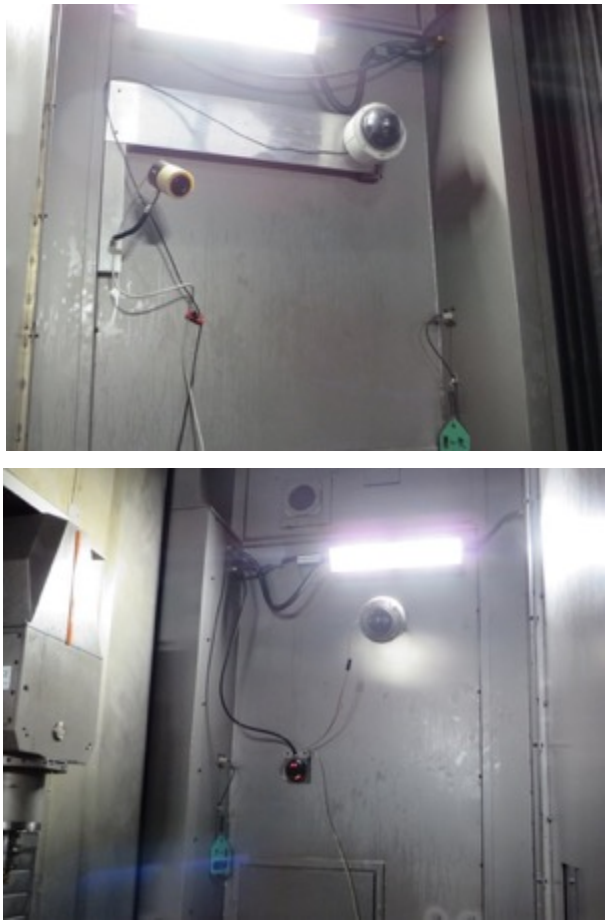

Figure 4.3. Visual camera and forward-looking IR camera setup, as deployed during hybrid AM. process.

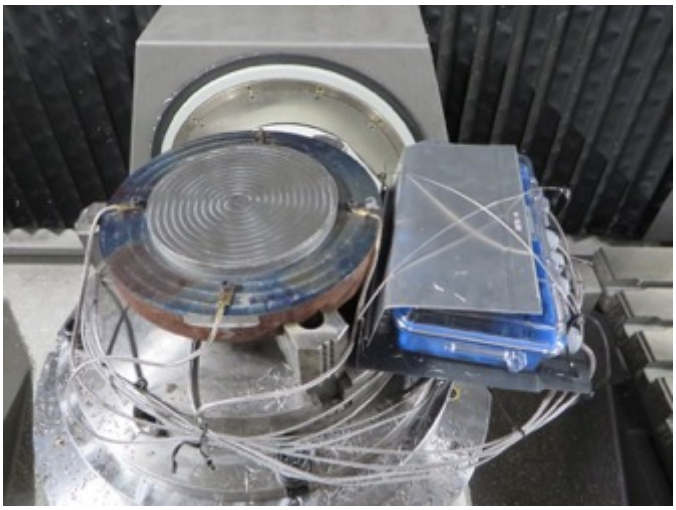

Figure 4.4. Setup for four standard K-Type thermocouples (one in each quadrant) that were attached to the build plate.

The end goal for using all these in situ monitoring tools, along with high-resolution imaging of the part, is to readily identify build defects such as delamination, excessive spatter, large surface cracking, or other process irregularities. This goal is essential for post-build evaluation and root cause analyses, as well as a course correction during the fabrication process. The second strategy is particularly relevant for hybrid AM, in which in situ defect identification provides an opportunity to initiate a machining operation to remove unwanted sections of the build [81].

4.4 IN SITU MONITORING CAPABILITIES IN BLOWN POWDER DIRECTED ENERGY DEPOSITION MACHINE

The AddUp BeAM Modulo 400 blown powder DED system was equipped with a standard melt pool monitoring capability. The imaging module for thermal profiles and geometric distortion information had three functions: (1) retrieve 3D geometry of objects at a high frame rate, (2) monitor the thermal gradient in space, and (3) measure in situ strain using digital image correlation [88]. Four sets of cameras were used, and illumination was provided in the four corners of the build chamber, which is sufficiently compact so as to not interfere with operation of the machine (Figure 4.5). Each of the four sensor systems consisted of (1) two 20 megapixel rolling shutter visible cameras capable of capturing frames at 18 Hz and spectrally filtered with a broad bandpass filter to a 440–555 nm wavelength region with fixed focal length lenses, (2) a FLIR Boson microbolometer long-wave IR camera with a resolution of 640°ø512 pixels, (3) a 320 J Xenon strobe, and (4) a 60 W white light-emitting diode (LED) [69].

Systems were chosen and arranged to provide full coverage over a build volume of a 400 mm diameter at 400 mm tall, with a projected pixel size of less than 100 μm to ensure resolution of specular highlights from individual unmelted, adhered powder particles. The data analytics pipeline for the BeAM is still in the early stages of development. However, initial work has begun on extracting features from the on-axis melt pool camera with the eventual goal of correlating these in situ features with defects in the final part [88].

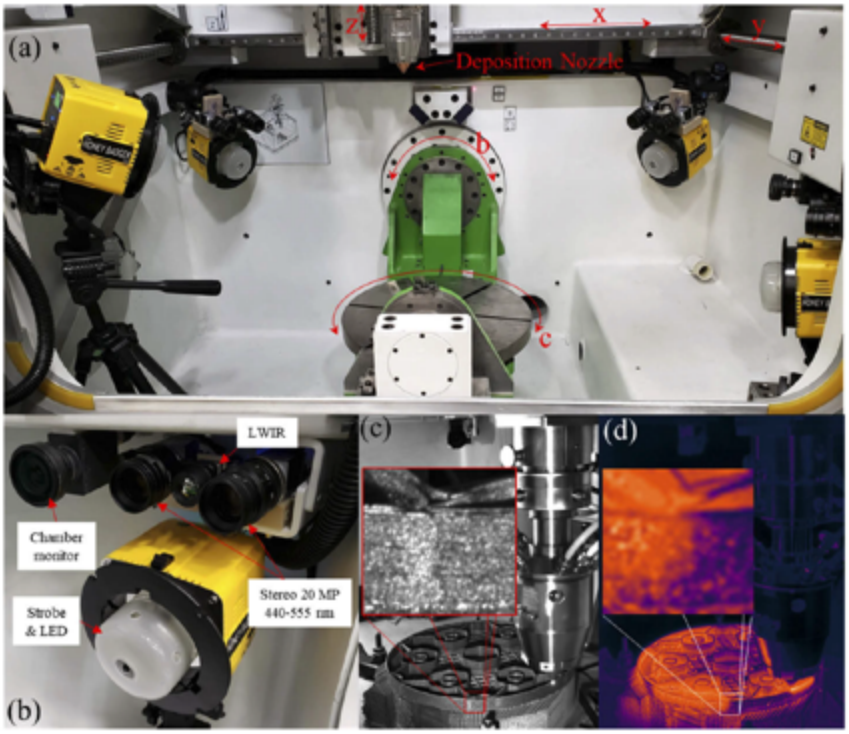

Figure 4.5. In situ differential interference contrast + IR setup in BeAM Modulo 400 system with (a) five-axis build chamber with four camera sets installed in corners. (b) Each camera set with two 20 megapixel visible-light cameras, one long-wave IR microbolometer camera, Xenon strobe light, and 60 W LED. (c) Single sample image from a visible camera under LED illumination, and (d) sample long-wave IR image showing thermal dissipation [69].

5. CONCLUSIONS

This report is a year one summary of a multiyear work package on the evaluation of large-scale AM challenges and opportunities for nuclear engineering components—primarily for pressure vessel applications—with an end goal of its certification and qualification. Three aspects of the report have been discussed in individual chapters: (1) literature review of structure–property relationships in mild steel and 316L SS alloys, which are the primary alloys used for nuclear part fabrication; (2) a summary of initial build success with symmetric/nonsymmetric, concentric, thin-walled structures (HIP can and t-valve geometry) using three distinctly different DED AM modalities—WAAM using the Lincoln Arc cell 1 machine, hybrid AM using Mazak machines, and BP-DED using the BeAM Modulo 400 machine; and (3) compilation of in situ monitoring capabilities such as thermocouple-based point probes, melt pool monitoring, and IR imaging, which was used for spatiotemporal data collection during the build process.

The literature review of structure–property relationships of mild steel and 316L parts is a key indicator that fully dense structures with subcritical flaw sizes may be fabricated by the DED AM technique. However, microstructures from the DED modality usually exhibit columnar grains along the build direction. This grain structure, along with preferred crystallographic texture (sometimes even possessing secondary texture), can lead to anisotropic mechanical properties in as-fabricated DED parts. The larger melt pool size in DED leads to significant thermal gradients (G) with high cooling rates (T), which favor columnar dendritic structures during the solidification process [89, 90]. Residual stress, which is a persistently observed phenomena in large-scale additive builds, needs to be mitigated to prevent deleterious effects such as distortion and cracking, delamination, and premature failure of parts.

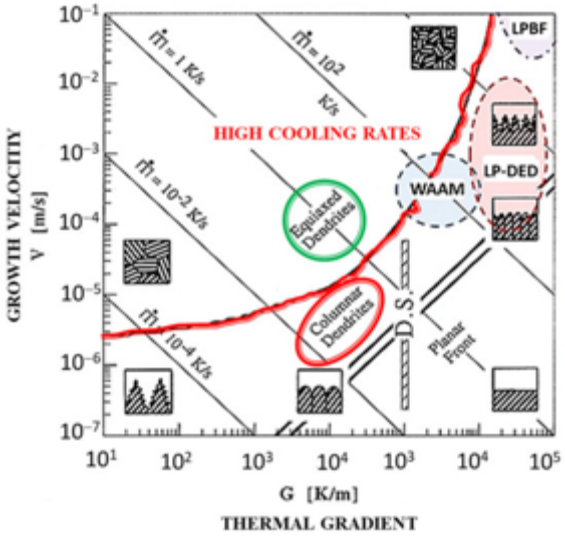

Figure 5.1. The DED process often leads to high cooling rates (T), growth velocities (v), and thermal gradients (G) and thus favors the formation of columnar grains [90].

The three different DED modalities explored in this work all have their advantages and disadvantages. The WAAM is really known for fast-paced fabrication of parts. In this case, the ability to produce concentric thin-wall (one bead width) builds with inward and outward inclination of the external wall was a great learning experience for the team. The ability to weld a plate on top to ensure a pressurized can environment was a successful feasibility demonstration for the WAAM process.

Similarly, the BP-DED modality is known for AM builds with better part resolution (compared with other wire-fed DED modalities) at the expense of relatively lower throughput. BP-DED has its unique

characteristics that could be a critical tool for feature addition, on-site repair with minimal thermal influence, and multimaterial builds. Overall, the ability to fabricate relatively fine features makes this modality quite distinct from other DED techniques.

Among the three DED modalities that were investigated, the hybrid AM technique using the Mazak machines showed the greatest potential for success. The ability to couple additive and subtractive manufacturing tools were a game changer to fabricate a fully enclosed t-valve structure (10.5 in. tall and 5.5 in. OD) that has sharp 90° angles with no support structures. Further trials are underway to fabricate full-scale AM t-valves with faster turnaround times.

Notably, the pressurized cans discussed in Chapter 3 are currently undergoing various steps of nondestructive evaluation, powder filling, and prepping processes. These parts would be shipped to an external vendor for conventional HIP trials. Pre- and post-HIP microstructure–property evaluations are planned for a few of these cans.

A key piece of this work package was to incorporate in situ sensing modalities that allow for a better understanding of the manufacturing process. Various probes were used to monitor the temperature, melt pool, IR emissions, and in some cases, distortion of the part. The data collected during all the builds are currently being postprocessed. This postprocessing is an essential step to parse, correlate, and finally prevent epistemic and aleatoric build variations that can cause microstructural abnormalities and introduce critical defects that are responsible for performance debits. This knowledge, when coupled with data analytics and advanced artificial intelligence tools, would be a significant step toward identifying defect signals and help with feed-forward corrections during large-scale complex AM builds in the future.

In summary, the journey ahead is exciting in the next couple of years of this work package, in line with the broader mission and vision of the Advanced Materials and Manufacturing Technologies Program. Some of the planned tasks include the evaluation of newer alloys, manufacturing larger-scale and more-complex pressure vessel geometries, and understanding the influence of additive characteristics such as surface roughness and structural integrity on post-HIP part performance.

6. REFERENCES

1. Hoelzer, D., *The Use of Powder Metallurgy and Hot Isostatic Pressing for Fabricating Components of Nuclear Power Plants*, ORNL/SPR-2022/2421 (Oak Ridge: Oak Ridge National Laboratory, 2022).
2. Love, L. J., Nycz, A., Noakes, M., Post, B., Roschli, A., and Babu, S. S., *Development and Demonstration of Large-Scale Metal Additive Manufacturing for Military Vehicle Applications*, ORNL/TM-2017/5 (Oak Ridge: Oak Ridge National Laboratory, 2016).
3. Office of Nuclear Energy, "4 Major Opportunities for Additive Manufacturing in Nuclear Energy," US Department of Energy, accessed on September 3, 2023, https://www.energy.gov/ne/articles/4-major-opportunities-additive-manufacturing-nuclear-energy.
4. Rostker, S., "Adding Up to Countdown: Additive Manufacturing and Its Implications for Nuclear Security," Center for Strategic and International Studies, accessed on September 3, 2023, https://www.csis.org/blogs/strategic-technologies-blog/adding-countdown-additive-manufacturing-and-its implications.
5. Betzler, B., "Additive Manufacturing in the Nuclear Reactor Industry," in Encyclopedia of Nuclear Energy (Cambridge, MA Press, 2021) 851–863.
6. Betzler, B. R., Ade, B. J., Wysocki, A. J., Jain, P. K., Chesser, P. C., Greenwood, M. S., and Terrani, K. A., "Transformational Challenge Reactor preconceptual core design studies," *Nuclear Engineering and Design* 367, 110781 (2020).
7. Gorelik, M., "Additive Manufacturing in the context of structural integrity", *Int. Jour. Of Fatigue* 94 (2017): 168–177.
8. Seifi, M., Gorelik, M., Waller, J., Hrabe, N., Shamsaei, N., Daniewicz, S., Lewandowski, J. J., "Progress Towards Metal Additive Manufacturing Standardization to Support Qualification and Certification," *JOM* 69, no. 3 (2017): 439–455.
9. Hull, A., "Review of Additive Manufacturing for Reactor Materials and Components," NRC Workshop on Vendor Oversight (www.nrc.gov/docs/ML1815/ML18150A363.pdf) (2018).
10. Gorelik, M., "Regulatory Considerations for AM and Status of the FAA AM Roadmap."
11. "What is Mild Steel? an in dept technical guide," metals4U, accessed on August 27, 2023, https://www.metals4u.co.uk/blog/mild-steel-in-depth-guide.
12. "The Iron Carbon Phase Diagram," accessed on August 27, 2023, https://www.tf.uni-kiel.de/matwis/amat/iss/kap_6/illustr/s6_1_2.html.
13. Suryakumar, S., Karunakaran, K. P., Chandrasekhar, U., Somashekara, M.A., "A study of the mechanical properties of objects built through weld-deposition," *Proceedings of the Institution of Mechanical Engineers, Part B: Journal of Engineering Manufacture* 227, no. 8 (2013):1138–1147.
14. Rafieazad, M., Ghaffari, M., Vahedi Nemani, A., Nasiri, A., "Microstructural evolution and mechanical properties of a low carbon low-alloy steel produced by wire arc additive manufacturing," *Int J Adv Manuf Technol* 105, no. 5–6 (2019): 2121–2134.
15. Sun, L., Jiang, F., Huang, R., Yuan, D., Guo, C., Wang, J., "Microstructure and mechanical properties of low-carbon high-strength steel fabricated by wire and arc additive manufacturing," *Metals* 10, no. 2 (2020): 216.
16. Soliman, M. A., *Phase transformations and mechanical properties of new austenite-stabilised Bainite Steels*, PhD Dissertation,

https://books.google.com/books/about/Phase_Transformations_and_Mechanical_Pro.html?id=hK9hzwEACAAJ (Pieper, 2008).

17. Colegrove, P. A., Coules, H. E., Fairman, J., Martina, F., Kashoob, T., Mamash, H., and Cozzolino, L. D., "Microstructure and residual stress improvement in wire and arc additively manufactured parts through high-pressure rolling," *J. Mater. Process. Technol*. 213, no. 10 (2013): 1782–1791.

18. Ding, J., Colegrove, P., Mehnen, J., Ganguly, S., Almeida Sequeira, P., Wang, F., and Williams, S., "Thermo-mechanical analysis of Wire and Arc Additive Layer Manufacturing process on large multi-layer parts," *Comput. Mater. Sci* 50, no. 12 (2011): 3315–3322.

19. Haden, C. V., Zeng, G., Carter III, F. M., Ruhl, C., Krick, B. A., and Harlow, D. G., "Wire and arc additive manufactured steel: Tensile and wear properties," *Additive Manufacturing* 16 (2017): 115–123.

20. Tang, W., Fancher, C. M., Nandwana, P., An, K., Nycz, A., Wang, H., Kannan, R., Trofimov, A., Yu, D., Leonard, D., Meyer, L., and Plotkowski, A., "Temperature-Dependent Thermal and Mechanical Properties of a Wire Arc Additively Manufactured Low Transformation Temperature Steel," *Met and Mat Trans. A* 54A (2023): 854–868.

21. Withers, P. J, and Bhadeshia, H. K. D. H., "Residual stress. Part 2—Nature and origins," *Mater. Sci. Technol.* 17 (2001): 366–375.

22. Dieter, G., *Metallurgy and Metallurgical Engineering Series* (New York: McGraw Hill Book Company, 1961).

23. Todd, R. I., Boccaccini, A. R., Sinclair, R., Yallee, R. B., Young, R. J., "Thermal residual stresses and their toughening effect in Al2O3 platelet reinforced glass," *Acta Mater*. 47 (1999): 3233–3240.

24. Shorr, B. F., *Thermal Integrity in Mechanics and Engineering* (Berlin/Heidelberg, Germany: Springer, 2015).

25. Withers, P. J., and Bhadeshia, H. K. D. H., "Residual stress. Part 1—Measurement techniques." *Mater. Sci. Technol.* 17 (2001): 355–365.

26. Rossini, N. S., Dassisti, M., Benyounis, K. Y., Olabi, A. G., "Methods for Measuring Residual Stresses in Components," *Mater. Des.* 35 (2012): 572–588.

27. Prado-Cerqueira, J. L., Camacho, A. M., Diéguez, J. L., Rodríguez-Prieto, A., Aragón, A. M., Lorenzo-Martín, C., and Yanguas-Gil, A., "Analysis of Favorable Process Conditions for the Manufacturing of Thin-Wall Pieces of Mild Steel Obtained by Wire and Arc Additive Manufacturing (WAAM)," *Materials* 11, no. 1449 (2018).

28. Shassere, B., Nycz, A., Noakes, M. W., Masuo, C., and Sridharan, N., "Correlation of Microstructure and Mechanical Properties of Metal Big Area Additive Manufacturing," *Appl. Sci*. 9, no. 787 (2019), DOI: 10.3390/app9040787.

29. https://bergsen.com/316-vs-316l-stainless-steel/

30. https://www.azom.com/article.aspx?ArticleID=2382

31. Saboori, A., Aversa, A., Bosio, F., Bassini, E., Librera, E., De Chirico, M., Biamino, S., Ugues, D., Fino, P., and Lombardi, M., "An investigation on the effect of powder recycling on the microstructure and mechanical properties of AISI 316L produced by Directed Energy Deposition," *Mater. Sci. Eng. A* 766, no. 138360 (2019).

32. Ma, M., Wang, Z., and Zeng, X., "A comparison on metallurgical behaviors of 316L stainless steel by selective laser melting and laser cladding deposition," *Mater. Sci. Eng. A* 685 (2017): 265–273.

33. Saboori, A., Aversa, A., Marchese, G., Biamino, S., Lombardi, M., and Fino, P., "Microstructure and Mechanical Properties of AISI 316L Produced by Directed Energy Deposition-Based Additive Manufacturing: A Review," *Appl. Sci.* 10, no. 3310 (2020), DOI: 10.3390/app10093310.

34. Bachmann, F., Hielscher, R., and Schaeben, H., "Texture analysis with MTEX—free and open source software toolbox," in *Texture and Anisotropy of Polycrystals III*, Solid State Phenomena vol. 160 (Trans Tech Publications Ltd, 2010), 63–68.

35. Van Nuland, T. F. W., Belotti, L. P., Hoefnagels, J. P. M., Van Dommelen, J. A. W., and Geers, M. G. D. "Microstructural modeling and measurements of anisotropic plasticity in large scale additively manufactured 316L stainless steel" *European Journal of Mechanics A: Solids* 96, no. 104710 (2022).

36. DebRoy, T., Wei, H. L., Zuback, J. S., Mukherjee, T., Elmer, J. W., Milewski, J. O., Beese, A. M., Wilson-Heid, A., De, A., and Zhang, W., "Additive manufacturing of metallic components—process, structure and properties," *Prog. Mater. Sci.* 92 (2018), 112–224.

37. Withers, P. J., and Bhadeshia, H. K. D. H., "Residual stress. Part 2 – _nature and origins," *Mater. Sci. Technol.* 17 (2001): 366–375, DOI: 10.1179/ 026708301101510087.

38. Saboori, A., Piscopo, G., Lai, M., Salmi, A., and Biamino, S., "An investigation on the effect of deposition pattern on the microstructure, mechanical properties and residual stress of 316L produced by Directed Energy Deposition," *Materials Science and Engineering A* 780, no. 139179 (2020).

39. Hietala, M., Rautio, T., Makikangas, J., Jaskari, M., Keskitalo, M., and Jarvenpaa, A., "Static Properties and Fatigue Strength of Wire Arc Additive Manufactured 316L," *7th Intl. Sci. Conf. on Applying New Technology in Green Buildings* (2022).

40. Palmeira Belotti, L., van Nuland, T. F. W., Geers, M. G. D., Ya, W., Hoefnagels, J. P. M., and van Dommelen, J. A. W., "On the anisotropy of wire arc additively manufactured parts," *Materials Science and Engineering A* 863, no. 144538 (2023).

41. "Directed Energy Deposition," ScienceDirect, https://www.sciencedirect.com/topics/materials-science/directed-energy-deposition.

42. Casalino, G., Karamimoghadam, M., and Contuzzi, N., "MetalWire Additive Manufacturing: A Comparison between Arc Laser and Laser/Arc Heat Sources," *Inventions* 8, no. 52 (2023), DOI: 10.3390/inventions8020052.

43. Alagha, A. N., Hussain, S., and Zaki, W., "Additive manufacturing of shape memory alloys: A review with emphasis on powder bed systems," *Mater. Des.* 204, no. 109654 (2021).

44. Seow, C. E., Zhang, J., Coules, H. E., Wu, G., Jones, C., Ding, J., and Williams, S. "Effect of crack-like defects on the fracture behaviour of Wire + Arc Additively Manufactured nickel-base Alloy 718," *Addit. Manuf.* 36, no. 101578 (2020).

45. Gao, Y., Wu, C., Peng, K., Song, X., Fu, Y., Chen, Q., Zhang, M., Wang, G., and Liu, J. "Towards superior fatigue crack growth resistance of TC4-DT alloy by in-situ rolled wire-arc additive manufacturing," *J. Mater. Res. Technol.* 15 (2021): 1395–1407.

46. Dharmendra, C., Shakerin, S., Ram, G. D. J., and Mohammadi, M., "Wire-arc additive manufacturing of nickel aluminum bronze/stainless steel hybrid parts—Interfacial characterization, prospects, and problems," *Materialia* 13, no. 100834 (2020).

47. Liu, R., Wang, Z., Sparks, T., Liou, F., and Newkirk, J. "Aerospace applications of laser additive manufacturing," in *Laser Additive Manufacturing* (Amsterdam, The Netherlands: Elsevier, 2017), 351–371.

48. Froes, F. H., Boyer, R. (Eds.), *Additive Manufacturing for the Aerospace Industry* (Amsterdam, The Netherlands: Elsevier, 2019).

49. Fu, J., Gong, L., Zhang, Y., Wu, Q., Shi, X., Chang, J., and Lu, J., "Microstructure and Mechanical Properties of Ti-6Al-4V Fabricated by Vertical Wire Feeding with Axisymmetric Multi-Laser Source," *Appl. Sci.* 7, no. 227 (2017).

50. Zhou, J., and Tsai, H.-L., "Porosity Formation and Prevention in Pulsed Laser Welding," *J. Heat Transf.* 129 (2006): 1014–1024.

51. Gennari, A., "Influence of Directed Energy Deposition (DED) parameters on microstructural features of AISI 316L steel," *Material Science* (2017).

52. Cunningham, C. R., Wikshåland, S., Xu, F., Kemakolam, N., Shokrani, A., Dhokia, V., and Newman, S. T., "Cost modelling and sensitivity analysis of wire and arc additive manufacturing," *Procedia Manuf.* 11 (2017): 650–657.

53. Venturini, G., Montevecchi, F., Bandini, F., Scippa, A., and Campatelli, G., "Feature based three axes computer aided manufacturing software for wire arc additive manufacturing dedicated to thin walled components," *Addit. Manuf.* 22 (2018): 643–657.

54. Williams, S. W., Martina, F., Addison, A. C., Ding, J., Pardal, G., and Colegrove, P., "Wire + arc additive manufacturing," *Mater. Sci. Technol.* 32 (2016): 641–647.

55. "MX3D: A smarter bridge," MX3D, accessed on 3 August 3, 2018, http://mx3d.com/smart-bridge/.

56. Bekker, A. C. M., and Verlinden, J. C., "Life cycle assessment of wire + arc additive manufacturing compared to green sand casting and CNC milling in stainless steel," *J. Clean. Prod.* 177 (2018): 438–447.

57. Ding, D. H., Pan, Z. X., Cuiuri, D., and Li, H. J., "Wire-feed additive manufacturing of metal components: technologies, developments and future interests," *Int. J. Adv. Manuf. Technol.* 81 (2015): 465–481.

58. Geng, H. B., Li, J. L., Xiong, J. T., Lin, X., and Zhang, F. S., "Optimization of wire feed for GTAW based additive manufacturing," *J. Mater. Process. Technol.* 243 (2017): 40–47.

59. Venturini, G., Montevecchi, F., Scippa, A., and Campatelli, G., "Optimization of WAAM Deposition Patterns for T-crossing Features," *Procedia CIRP* 55 (2016): 95–100.

60. Nycz, A., Adediran, A. I, Noakes, M. W., and Love, L. J., *Large Scale Metal Additive Techniques Review* (Oak Ridge: Oak Ridge National Laboratory Manufacturing Demonstration Facility, 2016).

61. Frazier, W. E., "Metal additive manufacturing: a review," *Journal of Materials Engineering and Performance* 23, no. 6 (2014): 1917–1928.

62. Nycz, A., Noakes, M. W., Richardson, B., Messing, A., Post, B., Paul, J., Flamm, J., and Love, L. J. "Challenges in Making Complex Metal Large-Scale Parts for Additive Manufacturing: A Case Study on the Additive Manufacturing Excavator," *Solid Freeform Fabrication 2017: Proceedings of the 28th Annual International Solid Freeform Fabrication Symposium—An Additive Manufacturing Conference* (2017): 2024–2033.

63. Lincoln Electric, *LINCOLN ER70S-6* (Cleveland, Ohio: T. L. E. Company, 2016).

64. Nycz, A., Noakes, M., and Cader, M., "Additive Manufacturing—A New Challenge for Automation and Robotics," R. Szewczyk et al. (Eds.), *Automation 2018* (Springer, 2018), 3–13, DOI: 10.1007/978-3-319-77179-3_1.

65. "Modulo 400," AddUp, accessed on August 30, 2023, https://addupsolutions.com/machines/ded/modulo-400.

66. Wimer, J., *Towards Certification of Additively Manufactured Safety-critical Parts for the Department of The Air Force*, PhD thesis (Defense Technical Information Center, 2020), https://apps.dtic.mil/sti/citations/AD1112356.

67. Sames, W. J., List, F. A., Pannala, S., Dehoff, R. R., and Babu, S. S., "The Metallurgy and Processing Science of Metal Additive Manufacturing," *International Materials* 61, no. 5 (2016): 315–360.

68. Usha, S., "Chapter 12—In situ monitoring of metal additive manufacturing process: a review," in *Additive Manufacturing: A Tool for Industrial Revolution 4.0* (Woodhead Publishing Reviews: Mechanical Engineering Series, 2021), 275–299.

69. Haley, J., Leach, C., Jordan, B., Dehoff, R., and Paquit, V., "In-situ digital image correlation and thermal monitoring in directed energy deposition additive manufacturing," *Optics Express* 29, no. 7 (2021): 9927–9941.

70. Haley, J. C., Zheng, B., Bertoli, U. S., Dupuy, A. D., Schoenung, J. M., and Lavernia, E. J., "Working distance passive stability in laser directed energy deposition additive manufacturing," *Mater. Des.* 161 (2019): 86–94.

71. Lee, Y., Nordin, M., Babu, S. S., Farson, D. F, "Effect of fluid convection on dendrite arm spacing in laser deposition," *Metall. Mater. Trans. B* 45, no. 4 (2014): 1520–1529.

72. Stender, M. E., Beghini, L. L., Sugar, J. D., Veilleux, M. G., Subia, S. R., Smith, T. R., San Marchi, C. W., Brown, A. A., and Dagel, D. J., "A thermal-mechanical finite element workflow for directed energy deposition additive manufacturing process modeling," *Addit. Manuf.* 21 (2018): 556–566.

73. Promoppatum, P., and Yao, S.-C., "Influence of scanning length and energy input on residual stress reduction in metal additive manufacturing: numerical and experimental studies," *J. Manuf. Process.* 49 (2020): 247–259.

74. Mukherjee, T., Zhang, W., and DebRoy, T., "An improved prediction of residual stresses and distortion in additive manufacturing," *Comput. Mater. Sci.* 126 (2017): 360–372.

75. Smith, T. R., Sugar, J. D., San Marchi, C., and Schoenung, J. M., "Strengthening mechanisms in directed energy deposited austenitic stainless steel," *Acta Mater.* 164 (2019): 728–740.

76. Everton, S. K., Hirsch, M., Stravroulakis, P., Leach, R. K., and Clare, A. T., "Review of in-situ process monitoring and in-situ metrology for metal additive manufacturing," *Mater. Des.* 95 (2016): 431–445.

77. Shevchik, S. A., Masinelli, G., Kenel, C., Leinenbach, C., and Wasmer, K., "Deep learning for in situ and real-time quality monitoring in additive manufacturing using acoustic emission," *IEEE Trans. Ind. Inf.* 15, no. 9 (2019): 5194–5203.

78. Montazeri, M., Nassar, A. R., Dunbar, A. J., and Rao, P., "In-process monitoring of porosity in additive manufacturing using optical emission spectroscopy," *IISE Trans.* 52, no. 5 (2020): 500–515.

79. Ocylok, S., Alexeev, E., Mann, S., Weisheit, A., Wissenbach, K., and Kelbassa, I., "Correlations of melt pool geometry and process parameters during laser metal deposition by coaxial process monitoring," in *8th International Conference on Laser Assisted Net Shape Engineering* (2014), 56, M. Schmidt, F. Vollertsen, and M. Merklein, Eds. (Amsterdam: Elsevier Science, 2014), 228–238.

80. Donadello, S., Motta, M., Demir, A. G., and Previtali, B., "Coaxial laser triangulation for height monitoring in laser metal deposition," *Procedia CIRP* 74 (2018): 144–148.

81. Haley, J., Karandikar, J., Herberger, C., MacDonald, E., Feldhausen, T., and Lee, Y., "Review of In Situ Process Monitoring for Hybrid Directed Energy Deposition," submitted to the *SME Journal of Manufacturing Processes* (2023).

82. Hagenlocher, C., O'Toole, P., Xu, W., Brandt, M., Easton, M., and Molotnikov, A., "In process monitoring of the thermal profile during solidification in laser directed energy deposition of aluminum," *Additive Manufacturing Letters* 3 no. 100084 (2022).

83. Staudt, T., Eschner, E., and Schmidt, M., "Temperature determination in laser welding based upon a hyperspectral imaging technique," *CIRP Ann.* 68 (2019): 225–228.

84. Halisch, C., Radel, T., Tyralla, D., and Seefeld, T., "Measuring the melt pool size in a wire arc additive manufacturing process using a high dynamic range two-colored pyrometric camera," *Weld World* 64 (2020): 1349–1356.

85. Volpp, J., "Behavior of powder particles on melt pool surfaces," *Int. Jour. Adv. Manuf. Tech*. 102 (2019): 2201–2210.

86. Kriczky, D. A., Irwin, J., Reutzel, E. W., Michaleris, P., Nassar, A. R., and Craig, J., "3D spatial reconstruction of thermal characteristics in directed energy deposition through optical thermal imaging," *Jour. Mater. Process Tech.* 221 (2015): 172–186.

87. Fetni, S., Enrici, T. M., Niccolini, T., Tran, H. S., Dedry, O., Duchene, L., Mertens, A., and Habraken, A. M., "Thermal model for the directed energy deposition of composite coatings of 316L stainless steel enriched with tungsten carbides," *Materials and Design* 204 (2021), 109661.

88. Scime, L., Haley, J., and Paquit, V., *Monitoring for Additive Manufacturing Technologies: Report on Progress, Achievements, and Limitations of Monitoring Techniques*, ORNL/SPR-2019/1354, TCR-DP-RPRT-001 (Oak Ridge: Oak Ridge National Laboratory, 2019).

89. Ozel, T., Shokri, H., and Loizeau, R., "A Review on Wire-Fed Directed Energy Deposition Based Metal Additive Manufacturing," *Jour. Manuf. And Matls. Proc.* 7, no. 45 (2023), DOI: 10.3390/jmmp7010045.

90. St. John, D. H., McDonald, S. D., Bermingham, M. J., Mereddy, S., Prasad, A., and Dargusch, M., "The challenges associated with the formation of equiaxed grains during additive manufacturing of titanium alloys," *Key Eng. Mater.* 770 (2018): 155–164.